Measurement of electrons from semileptonic heavy-flavor hadron decays in pp collisions at $\sqrt{s} = 7$ TeV

B. Abelev,[1] J. Adam,[2] D. Adamová,[3] A. M. Adare,[4] M. M. Aggarwal,[5] G. Aglieri Rinella,[6] A. G. Agocs,[7] A. Agostinelli,[8] S. Aguilar Salazar,[9] Z. Ahammed,[10] A. Ahmad Masoodi,[11] N. Ahmad,[11] S. A. Ahn,[12] S. U. Ahn,[13,14] A. Akindinov,[15] D. Aleksandrov,[16] B. Alessandro,[17] R. Alfaro Molina,[9] A. Alici,[18,19] A. Alkin,[20] E. Almaráz Aviña,[9] J. Alme,[21] T. Alt,[22] V. Altini,[23] S. Altinpinar,[24] I. Altsybeev,[25] C. Andrei,[26] A. Andronic,[27] V. Anguelov,[28] J. Anielski,[29] C. Anson,[30] T. Antičić,[31] F. Antinori,[32] P. Antonioli,[18] L. Aphecetche,[33] H. Appelshäuser,[34] N. Arbor,[35] S. Arcelli,[8] A. Arend,[34] N. Armesto,[36] R. Arnaldi,[17] T. Aronsson,[4] I. C. Arsene,[27] M. Arslandok,[34] A. Asryan,[25] A. Augustinus,[6] R. Averbeck,[27] T. C. Awes,[37] J. Äystö,[38] M. D. Azmi,[11] M. Bach,[22] A. Badalà,[39] Y. W. Baek,[13,14] R. Bailhache,[34] R. Bala,[17] R. Baldini Ferroli,[19] A. Baldisseri,[40] A. Baldit,[13] F. Baltasar Dos Santos Pedrosa,[6] J. Bán,[41] R. C. Baral,[42] R. Barbera,[43] F. Barile,[23] G. G. Barnaföldi,[7] L. S. Barnby,[44] V. Barret,[13] J. Bartke,[45] M. Basile,[8] N. Bastid,[13] S. Basu,[10] B. Bathen,[29] G. Batigne,[33] B. Batyunya,[46] C. Baumann,[34] I. G. Bearden,[47] H. Beck,[34] N. K. Behera,[48] I. Belikov,[49] F. Bellini,[8] R. Bellwied,[50] E. Belmont-Moreno,[9] G. Bencedi,[7] S. Beole,[51] I. Berceanu,[26] A. Bercuci,[26] Y. Berdnikov,[52] D. Berenyi,[7] A. A. E. Bergognon,[33] D. Berzano,[17] L. Betev,[6] A. Bhasin,[53] A. K. Bhati,[5] J. Bhom,[54] L. Bianchi,[51] N. Bianchi,[55] C. Bianchin,[56] J. Bielčík,[2] J. Bielčíková,[3] A. Bilandzic,[57,47] S. Bjelogrlic,[58] F. Blanco,[59] F. Blanco,[50] D. Blau,[16] C. Blume,[34] M. Boccioli,[6] N. Bock,[30] S. Böttger,[60] A. Bogdanov,[61] H. Bøggild,[47] M. Bogolyubsky,[62] L. Boldizsár,[7] M. Bombara,[63] J. Book,[34] H. Borel,[40] A. Borissov,[64] S. Bose,[65] F. Bossú,[51] M. Botje,[57] B. Boyer,[66] E. Braidot,[67] P. Braun-Munzinger,[27] M. Bregant,[33] T. Breitner,[60] T. A. Browning,[68] M. Broz,[69] R. Brun,[6] E. Bruna,[51,17] G. E. Bruno,[23] D. Budnikov,[70] H. Buesching,[34] S. Bufalino,[51,17] K. Bugaiev,[20] O. Busch,[28] Z. Buthelezi,[71] D. Caballero Orduna,[4] D. Caffarri,[56] X. Cai,[72] H. Caines,[4] E. Calvo Villar,[73] P. Camerini,[74] V. Canoa Roman,[75,76] G. Cara Romeo,[18] F. Carena,[6] W. Carena,[6] N. Carlin Filho,[77] F. Carminati,[6] C. A. Carrillo Montoya,[6] A. Casanova Díaz,[55] J. Castillo Castellanos,[40] J. F. Castillo Hernandez,[27] E. A. R. Casula,[78] V. Catanescu,[26] C. Cavicchioli,[6] C. Ceballos Sanchez,[79] J. Cepila,[2] P. Cerello,[17] B. Chang,[38,80] S. Chapeland,[6] J. L. Charvet,[40] S. Chattopadhyay,[10] S. Chattopadhyay,[65] I. Chawla,[5] M. Cherney,[81] C. Cheshkov,[6,82] B. Cheynis,[82] V. Chibante Barroso,[6] D. D. Chinellato,[83] P. Chochula,[6] M. Chojnacki,[58] S. Choudhury,[10] P. Christakoglou,[57,58] C. H. Christensen,[47] P. Christiansen,[84] T. Chujo,[54] S. U. Chung,[85] C. Cicalo,[86] L. Cifarelli,[8,6,19] F. Cindolo,[18] J. Cleymans,[71] F. Coccetti,[19] F. Colamaria,[23] D. Colella,[23] G. Conesa Balbastre,[35] Z. Conesa del Valle,[6] P. Constantin,[28] G. Contin,[74] J. G. Contreras,[75] T. M. Cormier,[64] Y. Corrales Morales,[51] P. Cortese,[87] I. Cortés Maldonado,[76] M. R. Cosentino,[67] F. Costa,[6] M. E. Cotallo,[59] E. Crescio,[75] P. Crochet,[13] E. Cruz Alaniz,[9] E. Cuautle,[88] L. Cunqueiro,[55] A. Dainese,[56,32] H. H. Dalsgaard,[47] A. Danu,[89] D. Das,[65] I. Das,[66] K. Das,[65] S. Dash,[90] A. Dash,[83] S. De,[10] G. O. V. de Barros,[77] A. De Caro,[91,19] G. de Cataldo,[92] J. de Cuveland,[22] A. De Falco,[78] D. De Gruttola,[91] H. Delagrange,[33] A. Deloff,[93] V. Demanov,[70] N. De Marco,[17] E. Dénes,[7] S. De Pasquale,[91] A. Deppman,[77] G. D Erasmo,[23] R. de Rooij,[58] M. A. Diaz Corchero,[59] D. Di Bari,[23] T. Dietel,[29] S. Di Liberto,[94] A. Di Mauro,[6] P. Di Nezza,[55] R. Divià,[6] Ø. Djuvsland,[24] A. Dobrin,[64,84] T. Dobrowolski,[93] I. Domínguez,[88] B. Dönigus,[27] O. Dordic,[95] O. Driga,[33] A. K. Dubey,[10] L. Ducroux,[82] P. Dupieux,[13] M. R. Dutta Majumdar,[10] A. K. Dutta Majumdar,[65] D. Elia,[92] D. Emschermann,[29] H. Engel,[60] H. A. Erdal,[21] B. Espagnon,[66] M. Estienne,[33] S. Esumi,[54] D. Evans,[44] G. Eyyubova,[95] D. Fabris,[56,32] J. Faivre,[35] D. Falchieri,[8] A. Fantoni,[55] M. Fasel,[27] R. Fearick,[71] A. Fedunov,[46] D. Fehlker,[24] L. Feldkamp,[29] D. Felea,[89] B. Fenton-Olsen,[67] G. Feofilov,[25] A. Fernández Téllez,[76] A. Ferretti,[51] R. Ferretti,[87] J. Figiel,[45] M. A. S. Figueredo,[77] S. Filchagin,[70] D. Finogeev,[96] F. M. Fionda,[23] E. M. Fiore,[23] M. Floris,[6] S. Foertsch,[71] P. Foka,[27] S. Fokin,[16] E. Fragiacomo,[97] U. Frankenfeld,[27] U. Fuchs,[6] C. Furget,[35] M. Fusco Girard,[91] J. J. Gaardhøje,[47] M. Gagliardi,[51] A. Gago,[73] M. Gallio,[51] D. R. Gangadharan,[30] P. Ganoti,[37] C. Garabatos,[27] E. Garcia-Solis,[98] I. Garishvili,[1] J. Gerhard,[22] M. Germain,[33] C. Geuna,[40] A. Gheata,[6] M. Gheata,[89,6] B. Ghidini,[23] P. Ghosh,[10] C. Di Giglio,[23] P. Gianotti,[55] M. R. Girard,[99] P. Giubellino,[6] E. Gladysz-Dziadus,[45] P. Glässel,[28] R. Gomez,[100] A. Gonschior,[27] E. G. Ferreiro,[36] L. H. González-Trueba,[9] P. González-Zamora,[59] S. Gorbunov,[22] A. Goswami,[101] S. Gotovac,[102] V. Grabski,[9] L. K. Graczykowski,[99] R. Grajcarek,[28] A. Grelli,[58] C. Grigoras,[6] A. Grigoras,[6] V. Grigoriev,[61] A. Grigoryan,[103] S. Grigoryan,[46] B. Grinyov,[20] N. Grion,[97] P. Gros,[84] J. F. Grosse-Oetringhaus,[6] J.-Y. Grossiord,[82] R. Grosso,[6] F. Guber,[96] R. Guernane,[35] C. Guerra Gutierrez,[73] B. Guerzoni,[8] M. Guilbaud,[82] K. Gulbrandsen,[47] T. Gunji,[104] A. Gupta,[53] R. Gupta,[53] H. Gutbrod,[27] Ø. Haaland,[24] C. Hadjidakis,[66] M. Haiduc,[89] H. Hamagaki,[104] G. Hamar,[7] B. H. Han,[105] L. D. Hanratty,[44] A. Hansen,[47] Z. Harmanova,[63] J. W. Harris,[4] M. Hartig,[34] D. Hasegan,[89] D. Hatzifotiadou,[18] A. Hayrapetyan,[6,103] S. T. Heckel,[34] M. Heide,[29] H. Helstrup,[21] A. Herghelegiu,[26] G. Herrera Corral,[75] N. Herrmann,[28] B. A. Hess,[106] K. F. Hetland,[21] B. Hicks,[4] P. T. Hille,[4] B. Hippolyte,[49] T. Horaguchi,[54] Y. Hori,[104]

P. Hristov,[6] I. Hřivnáčová,[66] M. Huang,[24] T. J. Humanic,[30] D. S. Hwang,[105] R. Ichou,[13] R. Ilkaev,[70] I. Ilkiv,[93] M. Inaba,[54] E. Incani,[78] G. M. Innocenti,[51] P. G. Innocenti,[6] M. Ippolitov,[16] M. Irfan,[11] C. Ivan,[27] V. Ivanov,[52] M. Ivanov,[27] A. Ivanov,[25] O. Ivanytskyi,[20] A. Jachołkowski,[6] P. M. Jacobs,[67] H. J. Jang,[12] S. Jangal,[49] M. A. Janik,[99] R. Janik,[69] P. H. S. Y. Jayarathna,[50] S. Jena,[90] D. M. Jha,[64] R. T. Jimenez Bustamante,[88] L. Jirden,[6] P. G. Jones,[44] H. Jung,[14] A. Jusko,[44] A. B. Kaidalov,[15] V. Kakoyan,[103] S. Kalcher,[22] P. Kaliňák,[41] T. Kalliokoski,[38] A. Kalweit,[107] K. Kanaki,[24] J. H. Kang,[80] V. Kaplin,[61] A. Karasu Uysal,[6,108] O. Karavichev,[96] T. Karavicheva,[96] E. Karpechev,[96] A. Kazantsev,[16] U. Kebschull,[60] R. Keidel,[109] P. Khan,[65] M. M. Khan,[11] S. A. Khan,[10] A. Khanzadeev,[52] Y. Kharlov,[62] B. Kileng,[21] D. W. Kim,[14] M. Kim,[14] M. Kim,[80] S. H. Kim,[14] D. J. Kim,[38] S. Kim,[105] J. H. Kim,[105] J. S. Kim,[14] B. Kim,[80] T. Kim,[80] S. Kirsch,[22] I. Kisel,[22] S. Kiselev,[15] A. Kisiel,[6,99] J. L. Klay,[110] J. Klein,[28] C. Klein-Bösing,[29] M. Kliemant,[34] A. Kluge,[6] M. L. Knichel,[27] A. G. Knospe,[111] K. Koch,[28] M. K. Köhler,[27] A. Kolojvari,[25] V. Kondratiev,[25] N. Kondratyeva,[61] A. Konevskikh,[96] A. Korneev,[70] R. Kour,[44] M. Kowalski,[45] S. Kox,[35] G. Koyithatta Meethaleveedu,[90] J. Kral,[38] I. Králik,[41] F. Kramer,[34] I. Kraus,[27] T. Krawutschke,[28,112] M. Krelina,[2] M. Kretz,[22] M. Krivda,[44,41] F. Krizek,[38] M. Krus,[2] E. Kryshen,[52] M. Krzewicki,[27] Y. Kucheriaev,[16] C. Kuhn,[49] P. G. Kuijer,[57] I. Kulakov,[34] J. Kumar,[90] P. Kurashvili,[93] A. B. Kurepin,[96] A. Kurepin,[96] A. Kuryakin,[70] V. Kushpil,[3] S. Kushpil,[3] H. Kvaerno,[95] M. J. Kweon,[28] Y. Kwon,[80] P. Ladrón de Guevara,[88] I. Lakomov,[66] R. Langoy,[24] S. L. La Pointe,[58] C. Lara,[60] A. Lardeux,[33] P. La Rocca,[43] C. Lazzeroni,[44] R. Lea,[74] Y. Le Bornec,[66] M. Lechman,[6] S. C. Lee,[14] K. S. Lee,[14] G. R. Lee,[44] F. Lefèvre,[33] J. Lehnert,[34] L. Leistam,[6] M. Lenhardt,[33] V. Lenti,[92] H. León,[9] M. Leoncino,[17] I. León Monzón,[100] H. León Vargas,[34] P. Lévai,[7] J. Lien,[24] R. Lietava,[44] S. Lindal,[95] V. Lindenstruth,[22] C. Lippmann,[27,6] M. A. Lisa,[30] L. Liu,[24] P. I. Loenne,[24] V. R. Loggins,[64] V. Loginov,[61] S. Lohn,[6] D. Lohner,[28] C. Loizides,[67] K. K. Loo,[38] X. Lopez,[13] E. López Torres,[79] G. Løvhøiden,[95] X.-G. Lu,[28] P. Luettig,[34] M. Lunardon,[56] J. Luo,[72] G. Luparello,[58] L. Luquin,[33] C. Luzzi,[6] R. Ma,[4] K. Ma,[72] D. M. Madagodahettige-Don,[50] A. Maevskaya,[96] M. Mager,[107,6] D. P. Mahapatra,[42] A. Maire,[28] M. Malaev,[52] I. Maldonado Cervantes,[88] L. Malinina,[46,*] D. Mal'Kevich,[15] P. Malzacher,[27] A. Mamonov,[70] L. Manceau,[17] L. Mangotra,[53] V. Manko,[16] F. Manso,[13] V. Manzari,[92] Y. Mao,[72] M. Marchisone,[13,51] J. Mareš,[113] G. V. Margagliotti,[74,97] A. Margotti,[18] A. Marín,[27] C. A. Marin Tobon,[6] C. Markert,[111] I. Martashvili,[114] P. Martinengo,[6] M. I. Martínez,[76] A. Martínez Davalos,[9] G. Martínez García,[33] Y. Martynov,[20] A. Mas,[33] S. Masciocchi,[27] M. Masera,[51] A. Masoni,[86] L. Massacrier,[82,33] M. Mastromarco,[92] A. Mastroserio,[23,6] Z. L. Matthews,[44] A. Matyja,[45,33] D. Mayani,[88] C. Mayer,[45] J. Mazer,[114] M. A. Mazzoni,[94] F. Meddi,[115] A. Menchaca-Rocha,[9] J. Mercado Pérez,[28] M. Meres,[69] Y. Miake,[54] L. Milano,[51] J. Milosevic,[95,†] A. Mischke,[58] A. N. Mishra,[101] D. Miśkowiec,[27,6] C. Mitu,[89] J. Mlynarz,[64] B. Mohanty,[10] A. K. Mohanty,[6] L. Molnar,[6] L. Montaño Zetina,[75] M. Monteno,[17] E. Montes,[59] T. Moon,[80] M. Morando,[56] D. A. Moreira De Godoy,[77] S. Moretto,[56] A. Morsch,[6] V. Muccifora,[55] E. Mudnic,[102] S. Muhuri,[10] M. Mukherjee,[10] H. Müller,[6] M. G. Munhoz,[77] L. Musa,[6] A. Musso,[17] B. K. Nandi,[90] R. Nania,[18] E. Nappi,[92] C. Nattrass,[114] N. P. Naumov,[70] S. Navin,[44] T. K. Nayak,[10] S. Nazarenko,[70] G. Nazarov,[70] A. Nedosekin,[15] M. Nicassio,[23] M. Niculescu,[89,6] B. S. Nielsen,[47] T. Niida,[54] S. Nikolaev,[16] V. Nikolic,[31] S. Nikulin,[16] V. Nikulin,[52] B. S. Nilsen,[81] M. S. Nilsson,[95] F. Noferini,[18,19] P. Nomokonov,[46] G. Nooren,[58] N. Novitzky,[38] A. Nyanin,[16] A. Nyatha,[90] C. Nygaard,[47] J. Nystrand,[24] A. Ochirov,[25] H. Oeschler,[107,6] S. Oh,[4] S. K. Oh,[14] J. Oleniacz,[99] C. Oppedisano,[17] A. Ortiz Velasquez,[84,88] G. Ortona,[51] A. Oskarsson,[84] P. Ostrowski,[99] J. Otwinowski,[27] K. Oyama,[28] K. Ozawa,[104] Y. Pachmayer,[28] M. Pachr,[2] F. Padilla,[51] P. Pagano,[91] G. Paić,[88] F. Painke,[22] C. Pajares,[36] S. Pal,[40] S. K. Pal,[10] A. Palaha,[44] A. Palmeri,[39] V. Papikyan,[103] G. S. Pappalardo,[39] W. J. Park,[27] A. Passfeld,[29] B. Pastirčák,[41] D. I. Patalakha,[62] V. Paticchio,[92] A. Pavlinov,[64] T. Pawlak,[99] T. Peitzmann,[58] H. Pereira Da Costa,[40] E. Pereira De Oliveira Filho,[77] D. Peresunko,[16] C. E. Pérez Lara,[57] E. Perez Lezama,[88] D. Perini,[6] D. Perrino,[23] W. Peryt,[99] A. Pesci,[18] V. Peskov,[6,88] Y. Pestov,[116] V. Petráček,[2] M. Petran,[2] M. Petris,[26] P. Petrov,[44] M. Petrovici,[26] C. Petta,[43] S. Piano,[97] A. Piccotti,[17] M. Pikna,[69] P. Pillot,[33] O. Pinazza,[6] L. Pinsky,[50] N. Pitz,[34] D. B. Piyarathna,[50] M. Płoskoń,[67] J. Pluta,[99] T. Pocheptsov,[46] S. Pochybova,[7] P. L. M. Podesta-Lerma,[100] M. G. Poghosyan,[6,51] K. Polák,[113] B. Polichtchouk,[62] A. Pop,[26] S. Porteboeuf-Houssais,[13] V. Pospíšil,[2] B. Potukuchi,[53] S. K. Prasad,[64] R. Preghenella,[18,19] F. Prino,[17] C. A. Pruneau,[64] I. Pshenichnov,[96] S. Puchagin,[70] G. Puddu,[78] J. Pujol Teixido,[60] A. Pulvirenti,[43,6] V. Punin,[70] M. Putiš,[63] J. Putschke,[64,4] E. Quercigh,[6] H. Qvigstad,[95] A. Rachevski,[97] A. Rademakers,[6] S. Radomski,[28] T. S. Räihä,[38] J. Rak,[38] A. Rakotozafindrabe,[40] L. Ramello,[87] A. Ramírez Reyes,[75] S. Raniwala,[101] R. Raniwala,[101] S. S. Räsänen,[38] B. T. Rascanu,[34] D. Rathee,[5] K. F. Read,[114] J. S. Real,[35] K. Redlich,[93,117] P. Reichelt,[34] M. Reicher,[58] R. Renfordt,[34] A. R. Reolon,[55] A. Reshetin,[96] F. Rettig,[22] J.-P. Revol,[6] K. Reygers,[28] L. Riccati,[17] R. A. Ricci,[118] T. Richert,[84] M. Richter,[95] P. Riedler,[6] W. Riegler,[6] F. Riggi,[43,39] B. Rodrigues Fernandes Rabacal,[6] M. Rodríguez Cahuantzi,[76] A. Rodriguez Manso,[57] K. Røed,[24] D. Rohr,[22] D. Röhrich,[24] R. Romita,[27] F. Ronchetti,[55] P. Rosnet,[13] S. Rossegger,[6] A. Rossi,[6,56] C. Roy,[49] P. Roy,[65] A. J. Rubio Montero,[59] R. Rui,[74] E. Ryabinkin,[16] A. Rybicki,[45] S. Sadovsky,[62] K. Šafařík,[6] R. Sahoo,[119] P. K. Sahu,[42] J. Saini,[10] H. Sakaguchi,[120] S. Sakai,[67] D. Sakata,[54] C. A. Salgado,[36] J. Salzwedel,[30] S. Sambyal,[53] V. Samsonov,[52] X. Sanchez Castro,[49] L. Šándor,[41]

A. Sandoval,[9] S. Sano,[104] M. Sano,[54] R. Santo,[29] R. Santoro,[92,6,19] J. Sarkamo,[38] E. Scapparone,[18] F. Scarlassara,[56] R. P. Scharenberg,[68] C. Schiaua,[26] R. Schicker,[28] C. Schmidt,[27] H. R. Schmidt,[106] S. Schreiner,[6] S. Schuchmann,[34] J. Schukraft,[6] Y. Schutz,[6,33] K. Schwarz,[27] K. Schweda,[27,28] G. Scioli,[8] E. Scomparin,[17] R. Scott,[114] P. A. Scott,[44] G. Segato,[56] I. Selyuzhenkov,[27] S. Senyukov,[87,49] J. Seo,[85] S. Serci,[78] E. Serradilla,[59,9] A. Sevcenco,[89] A. Shabetai,[33] G. Shabratova,[46] R. Shahoyan,[6] N. Sharma,[5] S. Sharma,[53] S. Rohni,[53] K. Shigaki,[120] M. Shimomura,[54] K. Shtejer,[79] Y. Sibiriak,[16] M. Siciliano,[51] E. Sicking,[6] S. Siddhanta,[86] T. Siemiarczuk,[93] D. Silvermyr,[37] C. Silvestre,[35] G. Simatovic,[88,31] G. Simonetti,[6] R. Singaraju,[10] R. Singh,[53] S. Singha,[10] V. Singhal,[10] T. Sinha,[65] B. C. Sinha,[10] B. Sitar,[69] M. Sitta,[87] T. B. Skaali,[95] K. Skjerdal,[24] R. Smakal,[2] N. Smirnov,[4] R. J. M. Snellings,[58] C. Søgaard,[47] R. Soltz,[1] H. Son,[105] M. Song,[80] J. Song,[85] C. Soos,[6] F. Soramel,[56] I. Sputowska,[45] M. Spyropoulou-Stassinaki,[121] B. K. Srivastava,[68] J. Stachel,[28] I. Stan,[89] I. Stan,[89] G. Stefanek,[93] T. Steinbeck,[22] M. Steinpreis,[30] E. Stenlund,[84] G. Steyn,[71] J. H. Stiller,[28] D. Stocco,[33] M. Stolpovskiy,[62] K. Strabykin,[70] P. Strmen,[69] A. A. P. Suaide,[77] M. A. Subieta Vásquez,[51] T. Sugitate,[120] C. Suire,[66] M. Sukhorukov,[70] R. Sultanov,[15] M. Šumbera,[3] T. Susa,[31] A. Szanto de Toledo,[77] I. Szarka,[69] A. Szczepankiewicz,[45] A. Szostak,[24] M. Szymanski,[99] J. Takahashi,[83] J. D. Tapia Takaki,[66] A. Tauro,[6] G. Tejeda Muñoz,[76] A. Telesca,[6] C. Terrevoli,[23] J. Thäder,[27] D. Thomas,[58] R. Tieulent,[82] A. R. Timmins,[50] D. Tlusty,[2] A. Toia,[22,6] H. Torii,[104] L. Toscano,[17] D. Truesdale,[30] W. H. Trzaska,[38] T. Tsuji,[104] A. Tumkin,[70] R. Turrisi,[32] T. S. Tveter,[95] J. Ulery,[34] K. Ullaland,[24] J. Ulrich,[122,60] A. Uras,[82] J. Urbán,[63] G. M. Urciuoli,[94] G. L. Usai,[78] M. Vajzer,[2,3] M. Vala,[46,41] L. Valencia Palomo,[66] S. Vallero,[28] N. van der Kolk,[57] P. Vande Vyvre,[6] M. van Leeuwen,[58] L. Vannucci,[118] A. Vargas,[76] R. Varma,[90] M. Vasileiou,[121] A. Vasiliev,[16] V. Vechernin,[25] M. Veldhoen,[58] M. Venaruzzo,[74] E. Vercellin,[51] S. Vergara,[76] R. Vernet,[123] M. Verweij,[58] L. Vickovic,[102] G. Viesti,[56] O. Vikhlyantsev,[70] Z. Vilakazi,[71] O. Villalobos Baillie,[44] A. Vinogradov,[16] L. Vinogradov,[25] Y. Vinogradov,[70] T. Virgili,[91] Y. P. Viyogi,[10] A. Vodopyanov,[46] K. Voloshin,[15] S. Voloshin,[64] G. Volpe,[23,6] B. von Haller,[6] D. Vranic,[27] G. Øvrebekk,[24] J. Vrláková,[63] B. Vulpescu,[13] A. Vyushin,[70] V. Wagner,[2] B. Wagner,[24] R. Wan,[49,72] M. Wang,[72] D. Wang,[72] Y. Wang,[28] Y. Wang,[72] K. Watanabe,[54] M. Weber,[50] J. P. Wessels,[6,29] U. Westerhoff,[29] J. Wiechula,[106] J. Wikne,[95] M. Wilde,[29] G. Wilk,[93] A. Wilk,[29] M. C. S. Williams,[18] B. Windelband,[28] L. Xaplanteris Karampatsos,[111] C. G. Yaldo,[64] Y. Yamaguchi,[104] H. Yang,[40] S. Yang,[24] S. Yasnopolskiy,[16] J. Yi,[85] Z. Yin,[72] I.-K. Yoo,[85] J. Yoon,[80] W. Yu,[34] X. Yuan,[72] I. Yushmanov,[16] C. Zach,[2] C. Zampolli,[18] S. Zaporozhets,[46] A. Zarochentsev,[25] P. Závada,[113] N. Zaviyalov,[70] H. Zbroszczyk,[99] P. Zelnicek,[60] I. S. Zgura,[89] M. Zhalov,[52] X. Zhang,[13,72] H. Zhang,[72] F. Zhou,[72] D. Zhou,[72] Y. Zhou,[58] J. Zhu,[72] J. Zhu,[72] X. Zhu,[72] A. Zichichi,[8,19] A. Zimmermann,[28] G. Zinovjev,[20] Y. Zoccarato,[82] M. Zynovyev,[20] and M. Zyzak[34]

(ALICE Collaboration)

[1]*Lawrence Livermore National Laboratory, Livermore, California, United States*
[2]*Faculty of Nuclear Sciences and Physical Engineering, Czech Technical University in Prague, Prague, Czech Republic*
[3]*Nuclear Physics Institute, Academy of Sciences of the Czech Republic, Řež u Prahy, Czech Republic*
[4]*Yale University, New Haven, Connecticut, United States*
[5]*Physics Department, Panjab University, Chandigarh, India*
[6]*European Organization for Nuclear Research (CERN), Geneva, Switzerland*
[7]*KFKI Research Institute for Particle and Nuclear Physics, Hungarian Academy of Sciences, Budapest, Hungary*
[8]*Dipartimento di Fisica dell'Università and Sezione INFN, Bologna, Italy*
[9]*Instituto de Física, Universidad Nacional Autónoma de México, Mexico City, Mexico*
[10]*Variable Energy Cyclotron Centre, Kolkata, India*
[11]*Department of Physics Aligarh Muslim University, Aligarh, India*
[12]*Korea Institute of Science and Technology Information, Daejeon, South Korea*
[13]*Laboratoire de Physique Corpusculaire (LPC), Clermont Université, Université Blaise Pascal, CNRS–IN2P3, Clermont-Ferrand, France*
[14]*Gangneung-Wonju National University, Gangneung, South Korea*
[15]*Institute for Theoretical and Experimental Physics, Moscow, Russia*
[16]*Russian Research Centre Kurchatov Institute, Moscow, Russia*
[17]*Sezione INFN, Turin, Italy*
[18]*Sezione INFN, Bologna, Italy*
[19]*Centro Fermi–Centro Studi e Ricerche e Museo Storico della Fisica "Enrico Fermi", Rome, Italy*
[20]*Bogolyubov Institute for Theoretical Physics, Kiev, Ukraine*
[21]*Faculty of Engineering, Bergen University College, Bergen, Norway*
[22]*Frankfurt Institute for Advanced Studies, Johann Wolfgang Goethe-Universität Frankfurt, Frankfurt, Germany*
[23]*Dipartimento Interateneo di Fisica 'M. Merlin' and Sezione INFN, Bari, Italy*
[24]*Department of Physics and Technology, University of Bergen, Bergen, Norway*

[25]*V. Fock Institute for Physics, St. Petersburg State University, St. Petersburg, Russia*
[26]*National Institute for Physics and Nuclear Engineering, Bucharest, Romania*
[27]*Research Division and ExtreMe Matter Institute EMMI, GSI Helmholtzzentrum für Schwerionenforschung, Darmstadt, Germany*
[28]*Physikalisches Institut, Ruprecht-Karls-Universität Heidelberg, Heidelberg, Germany*
[29]*Institut für Kernphysik, Westfälische Wilhelms-Universität Münster, Münster, Germany*
[30]*Department of Physics, Ohio State University, Columbus, Ohio, United States*
[31]*Rudjer Bošković Institute, Zagreb, Croatia*
[32]*Sezione INFN, Padova, Italy*
[33]*SUBATECH, Ecole des Mines de Nantes, Université de Nantes, CNRS-IN2P3, Nantes, France*
[34]*Institut für Kernphysik, Johann Wolfgang Goethe-Universität Frankfurt, Frankfurt, Germany*
[35]*Laboratoire de Physique Subatomique et de Cosmologie (LPSC), Université Joseph Fourier, CNRS-IN2P3, Institut Polytechnique de Grenoble, Grenoble, France*
[36]*Departamento de Física de Partículas and IGFAE, Universidad de Santiago de Compostela, Santiago de Compostela, Spain*
[37]*Oak Ridge National Laboratory, Oak Ridge, Tennessee, United States*
[38]*Helsinki Institute of Physics (HIP) and University of Jyväskylä, Jyväskylä, Finland*
[39]*Sezione INFN, Catania, Italy*
[40]*Commissariat à l'Energie Atomique, IRFU, Saclay, France*
[41]*Institute of Experimental Physics, Slovak Academy of Sciences, Košice, Slovakia*
[42]*Institute of Physics, Bhubaneswar, India*
[43]*Dipartimento di Fisica e Astronomia dell'Università and Sezione INFN, Catania, Italy*
[44]*School of Physics and Astronomy, University of Birmingham, Birmingham, United Kingdom*
[45]*The Henryk Niewodniczanski Institute of Nuclear Physics, Polish Academy of Sciences, Cracow, Poland*
[46]*Joint Institute for Nuclear Research (JINR), Dubna, Russia*
[47]*Niels Bohr Institute, University of Copenhagen, Copenhagen, Denmark*
[48]*Indian Institute of Technology Bombay (IIT), Mumbai, India*
[49]*Institut Pluridisciplinaire Hubert Curien (IPHC), Université de Strasbourg, CNRS-IN2P3, Strasbourg, France*
[50]*University of Houston, Houston, Texas, United States*
[51]*Dipartimento di Fisica Sperimentale dell'Università and Sezione INFN, Turin, Italy*
[52]*Petersburg Nuclear Physics Institute, Gatchina, Russia*
[53]*Physics Department, University of Jammu, Jammu, India*
[54]*University of Tsukuba, Tsukuba, Japan*
[55]*Laboratori Nazionali di Frascati, INFN, Frascati, Italy*
[56]*Dipartimento di Fisica dell'Università and Sezione INFN, Padova, Italy*
[57]*Nikhef, National Institute for Subatomic Physics, Amsterdam, Netherlands*
[58]*Nikhef, National Institute for Subatomic Physics and Institute for Subatomic Physics of Utrecht University, Utrecht, Netherlands*
[59]*Centro de Investigaciones Energéticas Medioambientales y Tecnológicas (CIEMAT), Madrid, Spain*
[60]*Institut für Informatik, Johann Wolfgang Goethe-Universität Frankfurt, Frankfurt, Germany*
[61]*Moscow Engineering Physics Institute, Moscow, Russia*
[62]*Institute for High Energy Physics, Protvino, Russia*
[63]*Faculty of Science, P.J. Šafárik University, Košice, Slovakia*
[64]*Wayne State University, Detroit, Michigan, United States*
[65]*Saha Institute of Nuclear Physics, Kolkata, India*
[66]*Institut de Physique Nucléaire d'Orsay (IPNO), Université Paris-Sud, CNRS-IN2P3, Orsay, France*
[67]*Lawrence Berkeley National Laboratory, Berkeley, California, United States*
[68]*Purdue University, West Lafayette, Indiana, United States*
[69]*Faculty of Mathematics, Physics and Informatics, Comenius University, Bratislava, Slovakia*
[70]*Russian Federal Nuclear Center (VNIIEF), Sarov, Russia*
[71]*Physics Department, University of Cape Town, iThemba LABS, Cape Town, South Africa*
[72]*Hua-Zhong Normal University, Wuhan, China*
[73]*Sección Física, Departamento de Ciencias, Pontificia Universidad Católica del Perú, Lima, Peru*
[74]*Dipartimento di Fisica dell'Università and Sezione INFN, Trieste, Italy*
[75]*Centro de Investigación y de Estudios Avanzados (CINVESTAV), Mexico City and Mérida, Mexico*
[76]*Benemérita Universidad Autónoma de Puebla, Puebla, Mexico*
[77]*Universidade de São Paulo (USP), São Paulo, Brazil*
[78]*Dipartimento di Fisica dell'Università and Sezione INFN, Cagliari, Italy*
[79]*Centro de Aplicaciones Tecnológicas y Desarrollo Nuclear (CEADEN), Havana, Cuba*
[80]*Yonsei University, Seoul, South Korea*
[81]*Physics Department, Creighton University, Omaha, Nebraska, United States*
[82]*Université de Lyon, Université Lyon 1, CNRS/IN2P3, IPN-Lyon, Villeurbanne, France*
[83]*Universidade Estadual de Campinas (UNICAMP), Campinas, Brazil*

[84]Division of Experimental High Energy Physics, University of Lund, Lund, Sweden
[85]Pusan National University, Pusan, South Korea
[86]Sezione INFN, Cagliari, Italy
[87]Dipartimento di Scienze e Innovazione Tecnologica dell'Università del Piemonte Orientale and Gruppo Collegato INFN, Alessandria, Italy
[88]Instituto de Ciencias Nucleares, Universidad Nacional Autónoma de México, Mexico City, Mexico
[89]Institute of Space Sciences (ISS), Bucharest, Romania
[90]Indian Institute of Technology, Mumbai, India
[91]Dipartimento di Fisica 'E.R. Caianiello' dell'Università and Gruppo Collegato INFN, Salerno, Italy
[92]Sezione INFN, Bari, Italy
[93]Soltan Institute for Nuclear Studies, Warsaw, Poland
[94]Sezione INFN, Rome, Italy
[95]Department of Physics, University of Oslo, Oslo, Norway
[96]Institute for Nuclear Research, Academy of Sciences, Moscow, Russia
[97]Sezione INFN, Trieste, Italy
[98]Chicago State University, Chicago, United States
[99]Warsaw University of Technology, Warsaw, Poland
[100]Universidad Autónoma de Sinaloa, Culiacán, Mexico
[101]Physics Department, University of Rajasthan, Jaipur, India
[102]Technical University of Split FESB, Split, Croatia
[103]Yerevan Physics Institute, Yerevan, Armenia
[104]University of Tokyo, Tokyo, Japan
[105]Department of Physics, Sejong University, Seoul, South Korea
[106]Eberhard Karls Universität Tübingen, Tübingen, Germany
[107]Institut für Kernphysik, Technische Universität Darmstadt, Darmstadt, Germany
[108]Yildiz Technical University, Istanbul, Turkey
[109]Zentrum für Technologietransfer und Telekommunikation (ZTT), Fachhochschule Worms, Worms, Germany
[110]California Polytechnic State University, San Luis Obispo, California, United States
[111]The University of Texas at Austin, Physics Department, Austin, TX, United States
[112]Fachhochschule Köln, Köln, Germany
[113]Institute of Physics, Academy of Sciences of the Czech Republic, Prague, Czech Republic
[114]University of Tennessee, Knoxville, Tennessee, United States
[115]Dipartimento di Fisica dell'Università 'La Sapienza' and Sezione INFN, Rome, Italy
[116]Budker Institute for Nuclear Physics, Novosibirsk, Russia
[117]Institut of Theoretical Physics, University of Wroclaw, Poland
[118]Laboratori Nazionali di Legnaro, INFN, Legnaro, Italy
[119]Indian Institute of Technology Indore (IIT), Indore, India
[120]Hiroshima University, Hiroshima, Japan
[121]Physics Department, University of Athens, Athens, Greece
[122]Kirchhoff-Institut für Physik, Ruprecht-Karls-Universität Heidelberg, Heidelberg, Germany
[123]Centre de Calcul de l'IN2P3, Villeurbanne, France

(Received 12 June 2012; published 20 December 2012)

The differential production cross section of electrons from semileptonic heavy-flavor hadron decays has been measured at midrapidity ($|y| < 0.5$) in proton-proton collisions at $\sqrt{s} = 7$ TeV with ALICE at the LHC. Electrons were measured in the transverse momentum range $0.5 < p_t < 8$ GeV/c. Predictions from a fixed-order perturbative QCD calculation with next-to-leading-log resummation agree with the data within the theoretical and experimental uncertainties.

DOI: 10.1103/PhysRevD.86.112007 PACS numbers: 13.85.Qk, 13.20.Fc, 13.20.He, 13.75.Cs

I. INTRODUCTION

The measurement of heavy-flavor (charm and beauty) production serves as an important testing ground of quantum chromodynamics (QCD), the theory of the strong interaction. Because of the large quark masses, heavy-flavor production in proton-proton (pp) collisions proceeds mainly through initial hard parton-parton collisions. Therefore, the production cross sections of charm and

*M. V. Lomonosov Moscow State University, D. V. Skobeltsyn Institute of Nuclear Physics, Moscow, Russia.
†University of Belgrade, Faculty of Physics and "Vinča" Institute of Nuclear Sciences, Belgrade, Serbia.

beauty quarks should provide a precision test of perturbative QCD (pQCD) for all values of transverse momenta p_t. In previous experiments with $p\bar{p}$ collisions at the Tevatron ($\sqrt{s} = 1.96$ TeV), charm production cross sections were measured at high p_t only and were found to exceed, by about 50% [1], the cross sections expected from pQCD calculations [2–4]. This, however, is still compatible with the substantial theoretical uncertainties. Beauty production at the Tevatron is well described by such calculations [5].

While the measurement of heavy-flavor production in pp collisions is important in its own interest, it also provides a crucial baseline for corresponding measurements in ultrarelativistic heavy-ion collisions. In such collisions a strongly interacting partonic medium is formed [6–9]. Heavy quarks interact with this medium after they have been produced in the initial stage of the collision. Consequently, heavy quarks suffer energy loss while they propagate through the medium, and they participate in the collective dynamics. The resulting modifications of the heavy-flavor momentum distributions in heavy-ion collisions with respect to those in pp collisions present a sensitive probe for the medium properties [10].

Heavy-flavor production can be investigated, among other channels, via the measurement of the contribution of semileptonic heavy-flavor decays to the inclusive lepton spectra. Both charm and beauty hadrons have substantial branching ratios ($\sim 10\%$) to single electrons or single muons [11], giving rise to a large ratio of signal leptons from heavy-flavor hadron decays to background from other lepton sources, in particular at high p_t.

Single electrons from heavy-flavor decays were first observed in the range $1.6 < p_t < 4.7$ GeV/c in pp collisions at the CERN ISR at $\sqrt{s} = 52.7$ GeV [12], before the actual discovery of charm. At the CERN Sp$\bar{p}$S, the UA1 experiment measured beauty production via single muons ($10 < p_t < 40$ GeV/c) at $\sqrt{s} = 630$ GeV [13], while the UA2 experiment used single electrons ($0.5 < p_t < 2$ GeV/c) to measure the charm production cross section [14]. At the Tevatron, both the CDF and D0 experiments measured beauty production via single electrons ($7 < p_t < 60$ GeV/c) [15] and single muons ($3.5 < p_t < 60$ GeV/c) [16], respectively.

At RHIC, semileptonic heavy-flavor decays were extensively studied in pp and, for the first time, in heavy-ion collisions, mainly in the electron channel. With the PHENIX experiment the range $0.3 < p_t < 9$ GeV/c was covered [17], and with the STAR experiment electrons from heavy-flavor hadron decays were measured in the range $3 < p_t < 10$ GeV/c [18]. Within experimental and theoretical uncertainties, pQCD calculations are in agreement with the measured production cross sections of electrons from charm [18,19] and beauty decays [20,21] at midrapidity in pp collisions at $\sqrt{s} = 0.2$ TeV. In Au-Au collisions, the total yield of electrons from heavy-flavor decays was observed to scale with the number of binary nucleon-nucleon collisions [22]. However, a strong suppression of the electron yield was discovered for $p_t > 2$ GeV/c [23,24] with a simultaneous observation of a nonzero electron elliptic flow strength v_2 for $p_t < 2$ GeV/c [10], indicating the substantial interaction of heavy quarks with the medium produced in Au-Au collisions at RHIC.

At the LHC, heavy-flavor production is studied in pp collisions at higher energies. Perturbative QCD calculations agree well with lepton production cross sections from heavy-flavor hadron decays measured for $p_t > 4$ GeV/c with the ATLAS experiment at $\sqrt{s} = 7$ TeV [25]. Furthermore, pQCD calculations of beauty hadron decays are in good agreement with production cross sections of nonprompt J/ψ at midrapidity as measured with the CMS experiment at high p_t ($p_t > 6.5$ GeV/c) [26] and with ALICE (A Large Ion Collider Experiment) at lower p_t ($p_t > 1.3$ GeV/c) [27]. D-meson production cross sections measured with ALICE are reproduced by corresponding calculations within substantial uncertainties at 7 [28] and at 2.76 TeV [29]. In addition, pQCD calculations are in agreement with the spectra of muons from heavy-flavor hadron decays at moderate p_t as measured with ALICE at 7 [30] and at 2.76 TeV [31]. It is of particular importance to investigate charm production at low p_t [28] in order to measure the total charm production cross section with good precision. Furthermore, low-p_t charm measurements at the LHC probe the parton distribution function of the proton in the region of parton fractional momenta $x \sim 10^{-4}$ and squared momentum transfers $Q^2 \sim (4\ \text{GeV})^2$, where gluon saturation effects might play a role [32].

This paper presents a measurement of single electrons, $(e^+ + e^-)/2$, from semileptonic decays of charm and beauty hadrons in the transverse momentum range $0.5 < p_t < 8$ GeV/c at midrapidity ($|y| < 0.5$) in pp collisions at $\sqrt{s} = 7$ TeV with ALICE. For such a measurement an excellent electron identification (eID) and precise knowledge of the remaining hadron background in the electron candidate sample are mandatory. Two complementary eID approaches are employed. Both are based on the particle specific energy loss dE/dx in the ALICE Time Projection Chamber, required to be compatible with the energy loss of electrons. To increase the purity of the electron candidate sample, in the first approach a combination of time-of-flight measurements and the response of the transition radiation detector is employed (TPC-TOF/TPC-TRD-TOF analysis). In the second approach, electromagnetic calorimetry is used (TPC-EMCal analysis).

This article is organized as follows: Sec. II gives an overview of the ALICE detector systems that are relevant for the analysis presented here. The details of the data

analysis are described in Sec. III. The differential production cross section of electrons from semileptonic heavy-flavor decays is presented in Sec. IV. In the same section, pQCD calculations at fixed order with next-to-leading-log resummation (FONLL [2,3,33]) are compared with the data, which extend the ATLAS measurement of electrons from heavy-flavor hadron decays to lower p_t. This article concludes with a summary in Sec. V.

II. ALICE SETUP

ALICE [34] is the experiment at the LHC dedicated to the study of heavy-ion collisions. The standard ALICE coordinate system is used, in which the interaction point (IP) where the particles collide is at the origin of a right-handed Cartesian coordinate system. From the IP the z axis is along the beam pipe, the x axis points towards the center of the LHC, ϕ is the azimuthal angle around the z axis, and θ is the polar angle with respect to this axis. The setup includes a muon spectrometer at backward pseudorapidity ($-4 < \eta < -2.5$) and a central barrel comprising several detector subsystems located inside a large solenoidal magnet. The magnet provides a uniform magnetic field of 0.5 T along the beam direction. Most of the barrel detectors have a common pseudorapidity coverage of $-0.9 < \eta < 0.9$. The apparatus is described in detail elsewhere [34]. In the following, the detectors used in the analysis are discussed briefly. For guidance, Fig. 1 shows a schematic beam view at $z = 0$ of the ALICE central barrel detectors during the 2010 running period of the LHC.

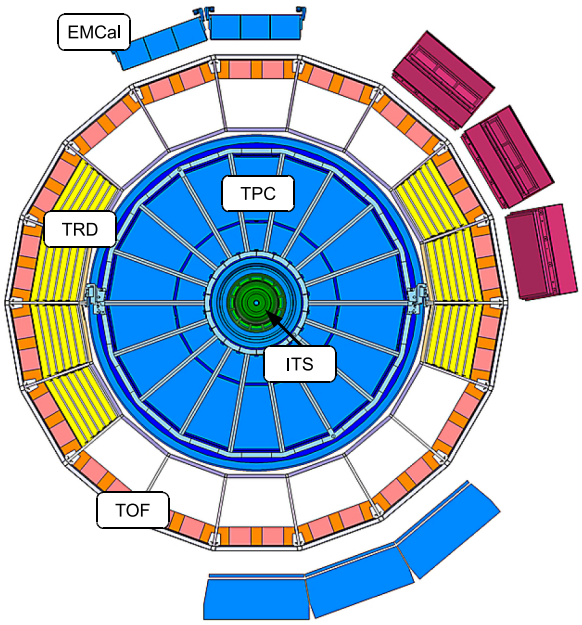

FIG. 1 (color online). Schematic beam view at $z = 0$ of the ALICE central barrel detectors during the 2010 running period of the LHC. The detectors used in the present analysis are the Inner Tracking System (ITS), the Time Projection Chamber (TPC), the Transition Radiation Detector (TRD), the Time-Of-Flight Detector (TOF), and the Electromagnetic Calorimeter (EMCal).

The vacuum beam pipe is made of beryllium with a thickness of 800 μm and an inner diameter of 58 mm. For protection the pipe is wrapped with polyimide with a thickness of about 80 μm. The corresponding material budget is 0.26% of a radiation length (X_0) at $\eta = 0$.

The beam pipe is surrounded by the Inner Tracking System (ITS). The ITS provides high-resolution space points for charged particle tracks close to the interaction point, thus improving the momentum and angular resolution. The ITS includes six cylindrical layers employing three different silicon detector technologies. The two innermost layers (at radii of 3.9 and 7.6 cm), which are equipped with Silicon Pixel Detectors (SPD), provide a spatial resolution of 12 μm in the plane perpendicular to the beam direction ($r\phi$) and 100 μm along the beam axis (z). About 83% of the SPD channels were operational for charged particle detection during the data-taking relevant for this analysis. The SPD also contributes to the collision trigger providing a fast estimation of the event multiplicity. The two intermediate layers of the ITS are built with Silicon Drift Detectors (SDD) and the two outermost layers consist of double-sided Silicon Strip Detectors (SSD). Their radii extend from 15 to 43 cm. The ITS modules were aligned using survey information, cosmic-ray tracks, and pp data with the methods described in Ref. [35]. The material budget of the entire ITS corresponds on average to about 7.18% of X_0 at $\eta = 0$ [34]. The exact knowledge of the material budget in the innermost ITS layers is crucial here as the conversion of photons into electron-positron pairs in material is the source of an important background component in the present analysis. In the ALICE experiment, the reconstruction of such conversion pairs has resulted in a measurement of the relevant material budget with a precision of 4.5% [36].

The most important detector for the track reconstruction and the momentum measurement is the Time Projection Chamber (TPC), which is also used for particle identification [37]. The ALICE TPC is a large cylindrical drift detector, whose active volume extends radially from 85 to 247 cm, and from -250 to $+250$ cm along the beam direction. The active volume of nearly 90 m^3 is filled with a Ne (85.5%), CO_2 (9.5%), and N_2 (4.8%) gas mixture. A central high-voltage electrode maintained at -100 kV divides the TPC into two sections. The end caps are equipped with multiwire proportional chambers with cathode pad readout. For a particle traversing the TPC, up to 159 space points (clusters) are recorded. The cluster data are used to reconstruct the charged particle trajectory in the magnetic field as well as to calculate the particle's specific energy loss $\mathrm{d}E/\mathrm{d}x$ in the TPC gas. Simultaneous measurements of the $\mathrm{d}E/\mathrm{d}x$ and momentum allow the identification of the particle species which has produced the track. The $\mathrm{d}E/\mathrm{d}x$ resolution of the TPC, $\sigma_{\text{TPC-d}E/\mathrm{d}x}$, was approximately 5.5% for minimum

ionizing particles crossing the full detector [38]. The dE/dx resolution was determined using minimum ionizing pions and cosmic ray muons at the Fermi plateau. Charged particle tracks are reconstructed in the ITS and TPC with a transverse momentum resolution ranging from about 1% at 1 GeV/c to about 3% at 10 GeV/c [37].

The TPC is surrounded by the Transition Radiation Detector (TRD) at a radial distance of 2.9 m from the beam axis. The TRD is segmented in the azimuth direction in 18 individual supermodules, seven of which were installed in the 2010 running period of ALICE as indicated in Fig. 1. Each supermodule is segmented further in five units (stacks) along the beam direction. Each stack comprises six layers in the radial direction. Each detector element consists of a fiber sandwich radiator of 48-mm thickness [39], a drift section of 30-mm thickness, and a multiwire proportional chamber section (7-mm thickness) with pad readout. The gas is a mixture of Xe (85%) and CO_2 (15%) [40–43]. The scope of the TRD is to provide a good separation of electrons from pions, particularly for momenta above 1 GeV/c. This is accomplished by measuring transition radiation photons, which are produced only by electrons [44]. The TRD is also designed to provide a fast trigger with particle identification information to discriminate electrons from hadrons [45]. This trigger was not used in the 2010 data-taking.

At larger radii, at a distance of 3.7 m from the beam axis, the Time-Of-Flight (TOF) detector provides further essential information for the particle identification. The TOF detector is segmented into 18 sectors and covers the full azimuth. Each sector contains 91 Multigap Resistive Plate Chambers (MRPCs). In total, 152,928 sensitive pads of dimension 2.5×3.5 cm^2 are read out. The TOF resolution of the particle arrival time is, at present, better than 100 ps [46]. The start time of the collision is measured by the ALICE T0 detector, an array of Cherenkov counters located at $+350$ and -70 cm along the beam line, or it is estimated using the particle arrival times at the TOF detector in events without a T0 signal. In the case that neither of the two methods provides an output, an average start time is used. Depending on the start time method used, the corresponding resolution is taken into account in the overall TOF PID resolution. The particle identification is based on the difference between the measured time of flight and its expected value, computed for each mass hypothesis from the track momentum and length of the trajectory. The overall resolution of this difference $\sigma_{\text{TOF-PID}}$ is about 160 ps [28].

The Electromagnetic Calorimeter (EMCal) is a Pb-scintillator sampling calorimeter, located at a radial distance of about 4.5 m from the beam line. The full detector covers the pseudorapidity range $-0.7 < \eta < 0.7$ with an azimuthal acceptance of $\Delta\phi = 107°$. In the 2010 running period of ALICE, the azimuthal coverage of the EMCal was limited to $\Delta\phi = 40°$, since only part of the detector was installed. The calorimeter is of the "Shashlik"-type built from alternating lead and scintillator segments of 1.44-and 1.76-mm thickness, respectively, together with longitudinal wavelength-shifting fibers for light collection. The cell size of the EMCal is approximately 0.014×0.014 rad in $\Delta\phi \times \Delta\eta$, and the depth corresponds to 20.1 X_0. From electron test beam data, the energy resolution of the EMCal was determined to be $1.7 \oplus 11.1/\sqrt{E(\text{GeV})} \oplus 5.1/E(\text{GeV})\%$ [47].

A minimum p_t of about 0.3 GeV/c is needed for the particles to reach the TRD, TOF, and EMCal detectors in the magnetic field of 0.5 T.

The VZERO detector is used for event selection and background rejection. It consists of two arrays of 32 scintillators each, which are arranged in four rings around the beam pipe on either side of the interaction region, covering the pseudorapidity ranges $2.8 < \eta < 5.1$ and $-3.7 < \eta < -1.7$, respectively. The time resolution of this detector is better than 1 ns. Information from the VZERO response is recorded in a time window of ± 25 ns around the nominal beam crossing time. The VZERO is used to select beam-beam interactions in the central region of ALICE and to discriminate against interactions of the beam with gas molecules in the beam pipe.

The ALICE minimum bias trigger required at least one hit in either of the two SPD layers or in the VZERO detector. In addition, collision events had to be in coincidence with signals from the beam position monitors, indicating the passage of proton bunches from both beams.

II. ANALYSIS

A. General strategy

For the measurement of the differential invariant cross section of electrons from semileptonic decays of heavy-flavor hadrons the following strategy was adopted. First, charged particle tracks which fulfil a set of electron identification cuts were selected. From the electron candidate tracks, the remaining contamination from misidentified hadrons was subtracted. After corrections for geometrical acceptance and efficiency, the inclusive electron yield per minimum bias triggered collision was determined for two different electron identification strategies. Since for all relevant sources the spectra of decay positrons and electrons are identical ($e^+/e^- = 1$), the average spectrum of positrons and electrons, $(e^+ + e^-)/2$, was used for the further analysis. The electron background from sources other than semileptonic heavy-flavor hadron decays was calculated using a cocktail approach and subtracted from the inclusive electron spectra. The resulting spectra of electrons from heavy-flavor hadron decays were normalized using the cross section of minimum bias triggered pp collisions. A weighted average of the two measurements obtained with different electron identification strategies led to the final result.

B. Data set and event selection

The data used in the present analysis were recorded during the 2010 running period. The luminosity was limited to $0.6 - 1.2 \times 10^{29}$ cm^{-2} s^{-1} in order to keep the probability of collision pileup per triggered event below 2.5%. This was cross-checked by looking at events with more than one vertex reconstructed with the SPD.

The primary collision vertex can be determined using the reconstructed tracks in the event or the correlated hits in the two pixel layers. Only events with a reconstructed primary vertex using one of the two methods were selected for further analysis. In order to minimize edge effects at the limit of the central barrel acceptance, the vertex was required to be within ± 10 cm from the center of the ALICE experiment along the beam direction. Integrated luminosities of 2.6 nb^{-1} and 2.1 nb^{-1} were used for the TPC-TOF/TPC-TRD-TOF and TPC-EMCal analysis, respectively.

In the offline analysis, pile-up events were identified using the SPD. Events with a second interaction vertex reconstructed with at least three tracklets (short tracks from SPD clusters) and well separated from the first vertex by more than 8 mm, are rejected from further analysis. Taking into account the efficiency of the pile-up event identification, less than 2.5% of the triggered events have been found to be related to more than one interaction. The effect of the remaining undetected pileup was negligible for the analysis. Moreover, background from beam-gas interactions was eliminated using the VZERO timing information as well as the correlation in the SPD between the number of reconstructed charged particle track segments and the number of hits.

C. Track reconstruction and selection

Charged particle tracks reconstructed in the TPC and ITS were propagated toward the outer detectors using a Kalman filter approach [48]. Geometrical matching was applied to associate tracks with hits in the outer detectors.

In the currently limited active area in azimuth of the TRD, the tracks were associated with track segments, called tracklets, reconstructed in individual chambers. This tracklet reconstruction assumed straight trajectories of charged particles passing a chamber. As the ALICE TRD comprises six layers, a track can include up to six tracklets. In the TPC-TRD-TOF analysis, a minimum of four associated TRD tracklets was required for each electron candidate track. For each tracklet the charge deposited in the corresponding chamber was measured. This information was used for electron identification.

The EMCal coverage was limited in the 2010 run. In azimuth, the installed EMCal sectors neither overlap with the installed TRD supermodules nor with the area of the innermost SPD layer which was operational in 2010 as indicated in Fig. 1. Electromagnetic showers reconstructed in the EMCal were associated with charged particle tracks if the distance between the track projection on the EMCal surface and the reconstructed shower was small in η and ϕ. The quadratic sum of the difference between track projection and reconstructed position had to be less than 0.05 in (η, ϕ) space for a track-shower pair to be accepted, where ϕ is measured in radians.

The pseudorapidity ranges used in the TPC-TOF/TPC-TRD-TOF and TPC-EMCal analyses were restricted to $|\eta| < 0.5$ and $|\eta| < 0.6$, respectively, because toward larger absolute values of η the systematic uncertainties related to particle identification increase considerably.

Electron candidate tracks were required to fulfil several track selection cuts. Table I summarizes these selection criteria. A cut on the χ^2 per degree of freedom (ndf) of the momentum fit in the TPC was applied to reject fake tracks which comprise a significant number of clusters originating from more than one charged particle trajectory. A track reconstructed within the TPC is characterized by the number of clusters used for the track reconstruction and fit (up to a maximum of 159 clusters). Not all of these clusters are used for the energy-loss calculation: those close to the borders of the TPC sectors are not considered. Separate cuts are applied on these two quantities. To guarantee good particle identification based on the specific dE/dx in the TPC, tracks were required to include a minimum number of 80 clusters used for the energy loss calculation. A cut on

TABLE I. Track selection cuts: except for the cut on the number of ITS hits and the request for hits in the SPD, the selections were common to all analysis strategies. See text for details.

Track property	Requirement
Number of TPC clusters	≥ 120
Number of TPC clusters used in the dE/dx calculation	≥ 80
Number of ITS hits in TPC-TOF/TPC-TRD-TOF	≥ 4
Number of ITS hits in TPC-EMCal	≥ 3
SPD layer in which a hit is requested in TPC-TOF/TPC-TRD-TOF	First
SPD layer in which a hit is requested in TPC-EMCal	Any
χ^2/ndf of the momentum fit in the TPC	<2
Distance of closest approach in xy (cm)	<1
Distance of closest approach in z (cm)	<2

the number of clusters for tracking is used to enhance the electron/pion separation. As the energy deposit of electrons on the Fermi plateau is approximately 1.6 times larger than for minimum ionizing particles, the associated clusters are insensitive to detector threshold effects and electron tracks have, on average, a higher number of clusters. The stringent request for at least 120 clusters from the maximum of 159 enhances electrons relative to hadrons.

Kink candidates, i.e., tracks which are not consistent with the track model of continuous particle trajectories but show deviations due to decays in flight or the emission of Bremsstrahlung, were discarded from further analysis since the $\mathrm{d}E/\mathrm{d}x$ resolution of the TPC is worse for such kink tracks than for regular tracks. In order to minimize the contribution from photon conversions in the ITS, a hit in the innermost SPD layer was required for all selected tracks in the TPC-TOF/TPC-TRD-TOF analysis. In total, at least four ITS hits were required to be associated with a track. Since the active area in azimuth of the EMCal overlapped with an inactive area of the first SPD layer, this approach had to be modified for the TPC-EMCal analysis. For the latter case, a matching hit was required in any of the two SPD layers and the required total number of ITS hits was reduced to three. Charged pion tracks from the weak decay $\mathrm{K}^0_\mathrm{S} \rightarrow \pi^+\pi^-$ occurring beyond the first SPD layer were used to demonstrate that the probability of random matches between tracks and uncorrelated hits in the ITS is negligible. A cut on the distance of closest approach (DCA) to the primary vertex in the transverse plane (xy) as well as in the beam direction (z) was applied to reject background tracks and nonprimary tracks.

D. Electron identification

Electrons were identified using the information provided by various detector subsystems of the ALICE central barrel. The detector which played the most important role in particle identification for both analyses discussed here is the TPC. Particle identification in the TPC is based on the measurement of the specific energy loss $\mathrm{d}E/\mathrm{d}x$ in the detector gas. The $\mathrm{d}E/\mathrm{d}x$ distribution, expressed in arbitrary units, as a function of the particle momentum for tracks measured in 7 TeV pp collisions, is shown in the left panel of Fig. 2. The solid lines depict the energy loss for electrons, pions, kaons, protons, and deuterons expected from the Bethe-Bloch formula [49]. For the electron selection, the energy loss was expressed as a deviation from the parametrized electron Bethe-Bloch line, divided by the energy-loss resolution $\sigma_{\text{TPC-d}E/\text{d}x}$, as shown in the right panel of Fig. 2.

Figure 2 demonstrates that the electron identification provided by the TPC is not sufficient at low momentum (below 1.5 GeV/c) because the kaon and proton $\mathrm{d}E/\mathrm{d}x$ lines cross the electron line. In addition, the merging of the $\mathrm{d}E/\mathrm{d}x$ lines of electrons, muons, pions, and other hadrons limits the particle identification at high momentum. Therefore, a high purity electron candidate sample can only be selected with the help of other detectors. Two different strategies were used in this analysis, one employing in addition the information from the TOF and TRD detectors, and the other one based on the EMCal response.

1. TPC-TOF/TPC-TRD-TOF analysis

The information provided by the TOF detector is complementary to that from the TPC in the low-momentum region, and it is used to resolve the ambiguities in the crossing regions of the TPC electron, kaon, and proton lines. The time-of-flight information allows the rejection of kaons up to a momentum of approximately 1.5 GeV/c and protons up to about 3 GeV/c. The selection was done by comparing the measured time of flight with the value expected assuming the particle being an electron. Only tracks compatible with the electron hypothesis within $3\sigma_{\text{TOF-PID}}$ were considered as electron candidates for further analysis. The difference between the measured time of flight and the expected time of flight, as a function of the

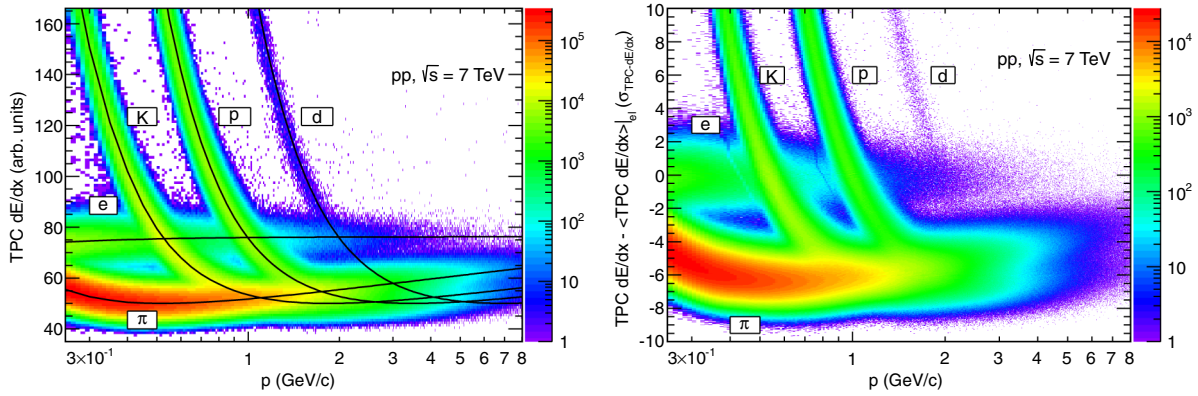

FIG. 2 (color online). Specific energy loss $\mathrm{d}E/\mathrm{d}x$ in arbitrary units measured in the TPC as a function of the reconstructed charged particle momentum (left panel) and expressed as a deviation from the expected energy loss of electrons, normalized by the energy-loss resolution (right panel). Contributions from both positively and negatively charged particles are included.

momentum, is shown in the upper left panel of Fig. 3. Lines indicate the selection band. This criterion combined with the selection of tracks between 0 and $3\sigma_{\text{TPC-d}E/\text{d}x}$ resulted in a pure sample of electron candidates up to a momentum of approximately 4 GeV/c. In this momentum range, the hadron contamination remained below 1%, while above 4 GeV/c the pion contamination became significant again. At such high momenta the TOF information could not be used to reduce further the hadron contamination in the electron candidate sample. Therefore, the TPC-TOF analysis was restricted to the p_{t} range below 4 GeV/c. To extend the accessible range to higher momenta, information from the TRD was used. As for the TPC, particle identification in the TRD makes use of the specific energy loss in the detector gas. In addition, the measurement of transition radiation photons produced by electrons traversing the dedicated radiators in front of the TRD drift chambers enhances distinctively the capability of the TRD to separate electrons from hadrons. The charge deposit per tracklet was compared with reference charge distributions obtained from dedicated test beam data [50], where electron and pion beams were provided at a number of different, discrete momenta. The probability of identifying a particle of given momentum as an electron was derived from a linear interpolation between the nearest measured data points in momentum. The electron probabilities were calculated for each TRD tracklet (up to six per track). They were combined for a given track and a likelihood value was calculated on which the eID is based.

The TRD electron likelihood distribution as a function of momentum for tracks passing the TOF selection and having six TRD tracklets is shown in the upper right panel of Fig. 3. The electron candidate selection was performed applying a momentum dependent cut defined such that it provided a constant electron efficiency of 80%. The p_{t} dependence of this cut was determined using a clean sample of electrons from photon conversions. Furthermore, this cut depends on the exact number of charge measurements (tracklets) available per track (four to six in the present analysis). The lower right panel of Fig. 3 depicts the cut described for six

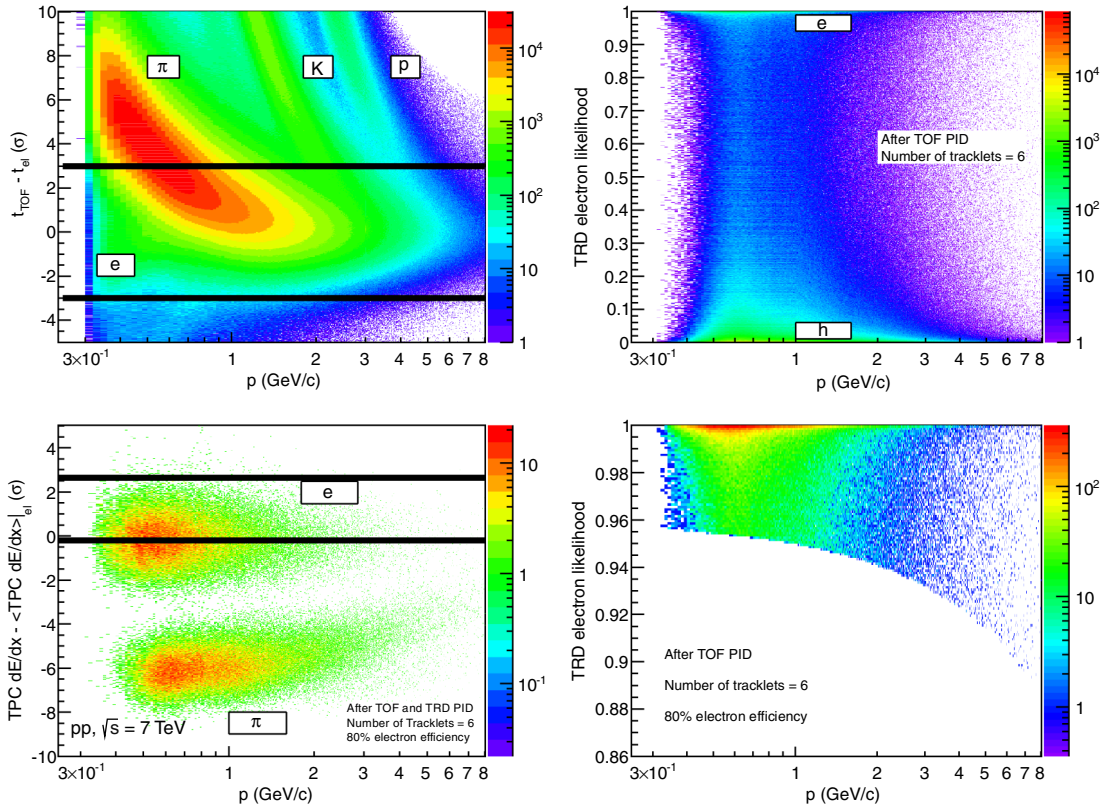

FIG. 3 (color online). Electron selection with the TOF, TRD, and TPC detectors. The difference between measured and expected time of flight is shown in the upper left panel. Lines indicate the selection band. For tracks selected by TOF, the TRD electron likelihood distribution for tracks with six TRD tracklets is shown in the upper right panel. The lower right panel displays the TRD electron likelihood distribution for tracks with an electron efficiency of 80% in the TRD (note the compressed scale on the vertical axis). For tracks passing the TRD selection, the TPC dE/dx, expressed in units of the dE/dx resolution ($\sigma_{\text{TPC-d}E/\text{d}x}$) is shown in the lower left panel. Lines indicate the electron selection band. The parametrization of the expected energy loss of electrons in this data period and the specific selection criteria of this analysis are such that the mean (width) of the electron dE/dx distribution is not exactly zero (one). Therefore, the selection band is slightly shifted from the nominal values of 0 and $3\sigma_{\text{TPC-d}E/\text{d}x}$.

tracklets. Cuts for tracks with four or five tracklets were applied in the same way. The TRD selection was applied only for tracks with a momentum above 4 GeV/c because at lower momenta the TPC-TOF selection was sufficient. For tracks passing the TRD selection, the lower left panel of Fig. 3 shows the particle dE/dx in the TPC, expressed as the distance to the expected energy deposit of electrons, normalized by the energy loss resolution. Having used the TRD information, an excellent separation of electrons from pions is already visible in the whole momentum range up to 8 GeV/c. The selection of tracks between 0 and $3\sigma_{\text{TPC-d}E/\text{d}x}$ results in an almost pure sample of electrons with a remaining hadron contamination of less than 2% over the full p_{t} range (see below).

2. TPC-EMCal analysis

An alternative approach to separate electrons from hadrons, over a wide momentum range, is based on electromagnetic calorimetry. Tracks were geometrically matched with clusters reconstructed in the EMCal. For each track, the momentum information was provided by the track reconstruction algorithms in the TPC and ITS. The corresponding energy deposit E was measured in the EMCal. The energy information was provided by a cluster of cells: the energy deposition was summed over adjacent cells, with an energy measurement above a threshold of ≈ 48 MeV around a seed cell.

For the TPC-EMCal analysis, tracks between -1.5 and $3\sigma_{\text{TPC-d}E/\text{d}x}$ were selected. For those candidate tracks, the ratio E/p of the energy deposited in the EMCal and the measured momentum was calculated to identify electrons. The distribution of E/p is shown in Fig. 4 for tracks with transverse momenta in the range $4 < p_{\text{t}} < 5$ GeV/c.

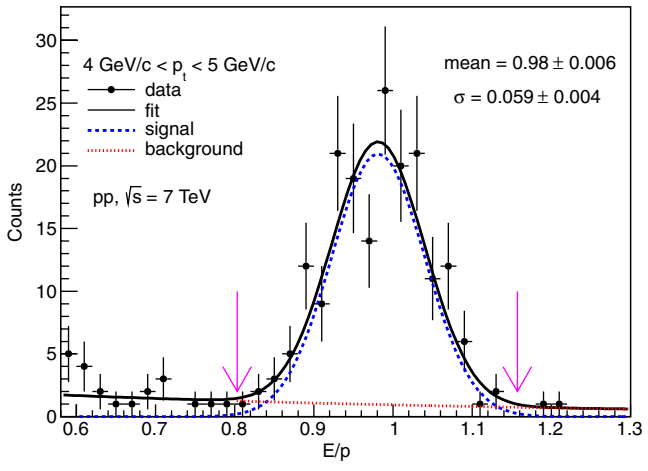

FIG. 4 (color online). Ratio E/p of the energy deposit in the EMCal and the measured momentum for charged particle tracks in the range $4 < p_{\text{t}} < 5$ GeV/c. The distribution was fitted with the sum of a Gaussian for the electron signal and an exponential for the remaining hadron background. Arrows indicate the selection window for electron candidates.

Electrons deposit their total energy in the EMCal and, due to their small mass, the ratio E/p should be equal to unity. Therefore, the peak around one in Fig. 4 confirms the good preselection of electron candidate tracks using the TPC. The exact shape of the E/p distribution depends on the EMCal response, Bremsstrahlung in the material crossed by electrons along their trajectory, and the remaining background from charged hadrons. The E/p distribution was fitted with the sum of a Gaussian and an exponential function. Electron candidates were required to have E/p between -3 and $+3\sigma_{E/p}$ of the E/p distribution, where $\sigma_{E/p}$ is the width of the fitted Gaussian function. Due to the loose ITS cuts, the TPC-EMCal analysis suffers from a large background from photon conversions and, consequently, a small signal- to-background ratio for electrons from heavy-flavor hadron decays at low p_{t}. Therefore, the p_{t} range was limited to $p_{\text{t}} > 3$ GeV/c, where a significant heavy-flavor signal could be measured.

E. Hadron contamination

The residual hadron contamination, after the electron identification cuts, was estimated by fitting the measured detector signal distributions with functions modelling the background and signal contributions. The hadron contamination is summarized in Table II for the three analysis strategies.

I. TPC-TOF/TPC-TRD-TOF analysis

For the TPC-TOF/TPC-TRD-TOF analysis, the TPC dE/dx distribution after TOF- and TRD-PID cuts was fitted in momentum slices. The residual contamination to the electron sample is given by the contribution of misidentified charged particles after the cut on the TPC dE/dx. The cut on the TPC dE/dx applied for electrons was chosen to have 50% efficiency for all momenta. The electron line was parametrized using a Gaussian function, which describes well the shape of the TPC dE/dx distribution, expressed as deviation from the parametrized electron Bethe-Bloch line normalized by the energy loss resolution, for a given particle species close to the maximum of this distribution. The dominant contribution to the contamination of the electron candidate sample at momenta above 1 GeV/c comes from the tail of the pion dE/dx distribution. This tail is not adequately described

TABLE II. Overview over the hadron contamination subtracted in the inclusive electron spectrum for the three analysis strategies.

Analysis	TPC-TOF	TPC-TRD-TOF	TPC-EMCal
p_{t} range (GeV/c)	0.5–4	4–8	3–7
Hadron contamination (%)	≤ 1	≤ 2	7 ± 4 (sys)

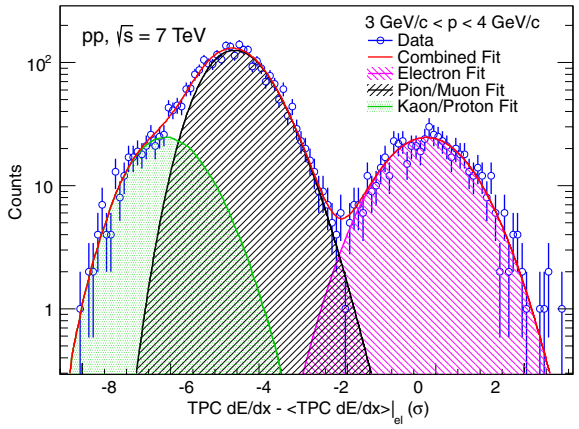

FIG. 5 (color online). The specific energy loss distribution measured with the TPC in the momentum range $3 < p < 4$ GeV/c (histogram) is compared to the sum of functions describing the contributions from different particle species. Data and fit agree within statistical uncertainties.

by a Gaussian for the purpose of an estimation of the contamination. A better description of the tail of the pion dE/dx distribution is obtained by multiplying a Landau distribution with an exponential term. The validity of this approach was confirmed using a clean pion sample from K^0_S decays which was selected using the V0-finder and tagged using topological cuts [51]. At low momenta, protons and kaons are suppressed by the eID cut applied using the TOF detector, while at higher momenta the kaon and proton dE/dx lines approach each other. Therefore, a single slightly skewed Gaussian distribution was used to fit the combined contribution of both particle types. The contribution of muons was fitted jointly with that of the pions.

The combined fit of the TPC dE/dx distribution in the momentum range $3 < p < 4$ GeV/c is shown in Fig. 5. To demonstrate that the fit does not introduce any additional systematic uncertainty, the difference between data and fit was compared with the expected statistical fluctuations. The fit is in good agreement with the data within statistical uncertainties.

The relative contamination was calculated as the ratio of the fitted background contribution to the overall distribution after the TPC dE/dx cut. The contamination remained insignificant (below 2%) up to a momentum of 8 GeV/c, and it was subtracted from the electron candidate sample in the TPC-TOF/TPC-TRD-TOF analysis.

2. TPC-EMCal analysis

For the TPC-EMCal analysis, the hadron contamination in the electron candidate sample was estimated based on fits to the E/p distribution in momentum slices with a function describing the signal (Gaussian for $E/p \sim 1$) and background (exponential) as shown in Fig. 4. Furthermore, the contamination has been constrained with the ratio of the integrals of the E/p distribution in two intervals: $\mu_{E/p}$ to $\mu_{E/p} + n \cdot \sigma_{E/p}$ and $\mu_{E/p} - n \cdot \sigma_{E/p}$ to $\mu_{E/p}$ for $n = 3$, where μ, σ are the parameters of the Gaussian and $\mu_{E/p}$ is the mean of the distribution. This ratio is sensitive to the amount of background in the measured E/p and its evolution has been studied by varying n between 1 and 3. Based on these estimates, the hadron contamination in the electron candidate sample was determined to be $(7 \pm 4)\%$ in the range $3 < p_t < 7$ GeV/c, and it was subtracted from the electron sample.

F. Corrections and normalization

Corrections were applied to the electron candidate spectra for the geometrical acceptance of the detectors (ϵ^{geo}), the reconstruction efficiency (ϵ^{reco}), and the electron identification efficiency (ϵ^{eID}).

Due to the finite azimuthal angle covered by the TRD and the EMCal detectors in the 2010 run, the maximum geometrical acceptance was 38% for the TPC-TRD-TOF analysis and 11% for the TPC-EMCal analysis. The geometrical acceptance and reconstruction efficiency were computed from a full numerical Monte Carlo simulation of the experiment. Monte Carlo events were produced by the PYTHIA 6.4.21 event generator [52] using the Perugia-0 parameter tuning [53] with the same primary vertex distribution as in the data. The generated particles were propagated through the apparatus using GEANT3 [54]. The same reconstruction algorithms and cuts were used as for the analysis of data. For the calculation of ϵ^{geo} and ϵ^{reco} in the TPC-TOF/TPC-TRD-TOF analysis, which requires a hit in the first SPD layer, only those electrons were considered in the simulation which were produced within 3 cm distance from the interaction vertex in the transverse direction and which were reconstructed in the pseudorapidity range $|\eta| < 0.5$. For the TPC-EMCal analysis, which requires a hit in any of the two SPD layers, electrons produced within 7 cm transverse distance from the vertex and with $|\eta| < 0.6$ were considered for the calculation of ϵ^{geo} and ϵ^{reco}.

The evaluation of the electron transverse momentum is affected by the finite momentum resolution and by the electron energy loss due to Bremsstrahlung in the material in front of and in the tracking detectors, where the dominant contribution is from the ITS ($X/X_0 = 7.18\%$ at $\eta = 0$ [34]). These effects distort the shape of the p_t distribution, which falls steeply with increasing momentum, and have to be taken into account. The necessary correction grows with increasing steepness of the p_t distribution and with increasing widths of the p_t bins. To determine this correction, an unfolding procedure based on Bayes's theorem was applied. The Monte Carlo generated and reconstructed transverse momentum distributions of electrons were used to obtain a smearing matrix. A detailed description of the procedure can be found elsewhere [55]. The

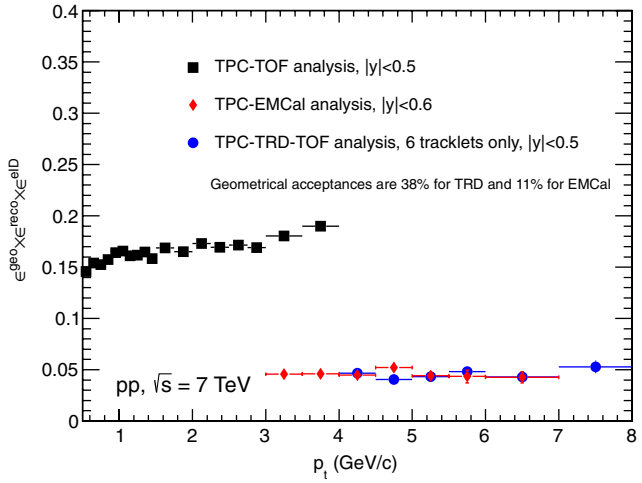

FIG. 6 (color online). Acceptance, tracking, and particle identification efficiency for electrons at midrapidity in pp collisions at 7 TeV for the TPC-TOF/TPC-TRD-TOF and the TPC-EMCal analysis. For transverse momenta below 4 GeV$/c$ the TRD was not used for eID. The total reconstruction efficiency for electrons with the TPC-TRD-TOF eID approach is shown for the requirement of six tracklets in the TRD as an example.

maximum unfolding correction of the measured electron yield was $\approx 20\%$ at $p_{\mathrm{t}} = 2$ GeV$/c$, becoming smaller towards higher p_{t}.

The product of the overall acceptance and efficiency ($\epsilon^{\mathrm{geo}} \times \epsilon^{\mathrm{reco}} \times \epsilon^{\mathrm{eID}}$) as a function of p_{t} for the TPC-TOF/TPC-TRD-TOF analysis as well as the overall efficiency for the TPC-EMCal analysis are shown in Fig. 6.

To cross-check the value of the acceptance times efficiency calculated via the simulation and to determine TRD PID efficiencies, a data-driven method was employed. A pure sample of electrons from photon conversions in the detector material was selected. Reconstructed conversion electron vertices were selected using the V0-finder [51]. The same cuts as in the analysis were applied to the pure electron sample except for the requirements in the ITS which were relaxed such that the electron candidates needed to have only two hits in the ITS, from which at least one is required to be in any of the two pixel layers. The cross-check was done in the momentum range where the sample of electrons from photon conversions is statistically significant (up to 6 GeV$/c$). The good agreement of the TRD acceptance and tracking efficiency ($\epsilon^{\mathrm{geo}}_{\mathrm{TRD}} \times \epsilon^{\mathrm{reco}}_{\mathrm{TRD}}$) for electrons from conversions in data and in the simulation, which have at least five TRD tracklets, is demonstrated in Fig. 7. The TOF tracking and PID efficiency after the TRD requirement ($\epsilon^{\mathrm{geo}}_{\mathrm{TOF}} \times \epsilon^{\mathrm{reco}}_{\mathrm{TOF}} \times \epsilon^{\mathrm{eID}}_{\mathrm{TOF}}$) is also well reproduced in the simulations (see Fig. 7).

For the TPC-EMCal analysis, the electron identification efficiency from the TPC d$E/$dx cut was estimated using the data-driven method. Particles were selected with a d$E/$dx in the range between -1.5 and 3 $\sigma_{\text{TPC-d}E/\text{d}x}$. The corresponding efficiency was about 93% with respect to the full distribution. The efficiency of the electron identification with EMCal, i.e., track matching and eID employing the E/p cut, was estimated using the simulation.

The p_{t}-differential invariant yield $N^{\mathrm{e}^{\pm}}$ of inclusive electrons, $(\mathrm{e}^{+} + \mathrm{e}^{-})/2$, was calculated from the corrected

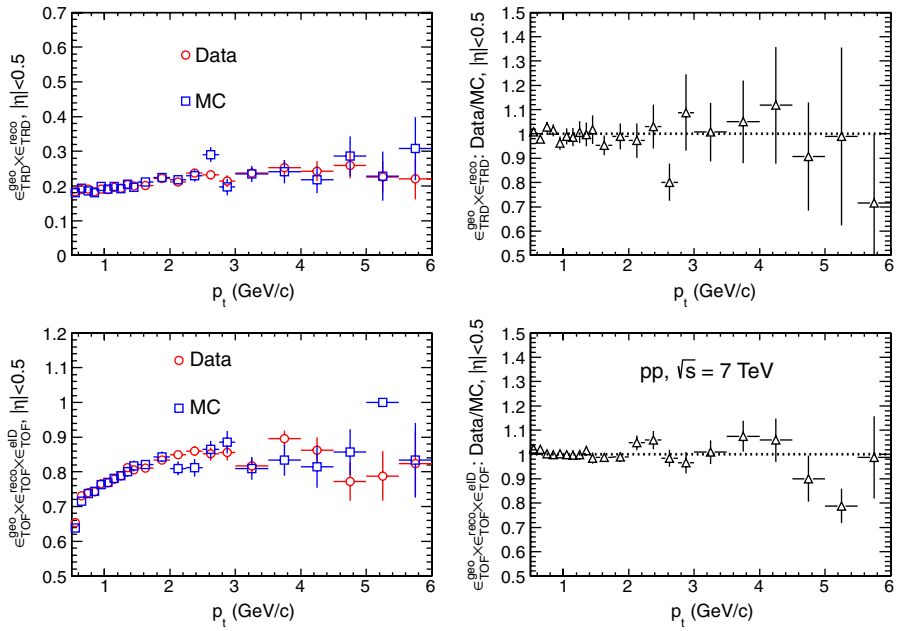

FIG. 7 (color online). Acceptance, tracking, and particle identification efficiencies are compared in data and in simulation for electrons from photon conversions in material. Upper panel: TRD acceptance times tracking efficiency (at least five reconstructed tracklets were required for this example). For transverse momenta below 4 GeV$/c$, the TRD was not used for eID. Lower panel: TOF matching efficiency times particle identification efficiency.

electron p_t spectrum and the number N_{MB} of minimum bias pp collisions as

$$\frac{1}{2\pi p_t}\frac{d^2N^{e^\pm}}{dp_t dy} = \frac{1}{2}\frac{1}{2\pi p_t^{centre}}\frac{1}{\Delta y \Delta p_t}\frac{N^{e^\pm}_{raw}(p_t)}{(\epsilon^{geo}\times\epsilon^{reco}\times\epsilon^{eID})} \times \frac{1}{N_{MB}}, \quad (1)$$

where p_t^{centre} are the centers of the p_t bins with widths Δp_t chosen here, and Δy is the width of the rapidity interval covered. In the following, invariant yields or cross sections within a given p_t bin are always quoted at the bin centre without a bin-shift correction for the fact that the electron yield decreases with increasing p_t. When ratios of yields or cross sections are calculated the same p_t bins are used for both the numerator and the denominator and average yields or cross sections are used for every individual p_t bin to avoid bin-shift effects.

G. Systematic uncertainties

1. TPC-TOF-TRD analysis

The following sources of systematic uncertainties were considered: the corrections of the ITS, TPC, TOF, and TRD tracking efficiencies, the TOF, TPC, and TRD particle identification efficiencies, the p_t unfolding procedure, and the absolute normalization.

To estimate the contributions from tracking and particle identification, the analysis was repeated with modified selection criteria as summarized in Table III.

For each variation of the selection criteria, the inclusive electron spectra were fully corrected. The resulting spectra were compared by inspecting their ratio. As a function of p_t, these ratios define the relative systematic uncertainties as listed in Table IV. A general systematic uncertainty of 2%, due to the ITS-TPC track matching efficiency, was taken from dedicated tracking investigations. It is important to note that for each cut related to the particle identification, the hadron contamination may change and has to be reevaluated.

In addition, the corrected spectra of positrons and electrons, as well as the corrected spectra obtained in the positive (η^+) and negative η (η^-) range, were compared. Deviations from the expected ratios $e^+/e^- = 1$ and $\eta^+/\eta^- = 1$ were taken into account in the systematics.

The systematic uncertainty related to the MC p_t-distribution used for the corrections, named "unfolding" in Table IV, was extracted from the comparison of the data corrected with two different Monte Carlo samples. In addition to the PYTHIA 6.4.21 based sample, used already for the evaluation of the geometrical acceptance and the reconstruction efficiency (see Sec. III F), a second PYTHIA based sample with artificially enhanced heavy-flavor hadron yields was employed.

Up to electron transverse momenta of 4 GeV/c, the electron identification was based on the TPC-TOF selection only. For higher momenta, the TRD selection was included. Therefore, the TRD contribution to the systematic uncertainties was only considered for the part of the spectrum above 4 GeV/c.

The systematic uncertainties are summarized in Table IV. The systematic uncertainty of the DCA cuts increases at low p_t, where the DCA resolution decreases, and electrons from photon conversion in the material do

TABLE III. Variation of the electron selection criteria to estimate the systematic uncertainties due to track reconstruction and particle identification.

Variable	Looser criteria	Reference criteria	Stronger criteria
All analyses:			
N. of TPC tracking clusters	≥ 100	≥ 120	≥ 140
N. of TPC PID clusters	≥ 80	≥ 80	≥ 100, ≥ 120
DCA to the primary vertex in xy (z)	<2 cm (<4 cm)	<1 cm (<2 cm)	<0.5 cm (<1 cm) <0.3 cm (<0.5 cm)
TPC-TOF and TPC-TRD-TOF analyses:			
Number of ITS hits	≥ 3	≥ 4	≥ 5
TOF compatibility with e hypothesis	$\leq 4\sigma_{\text{TOF-PID}}$	$\leq 3\sigma_{\text{TOF-PID}}$	$\leq 2\sigma_{\text{TOF-PID}}$
TPC dE/dx cut	$-0.254 < \sigma_{\text{TPC-d}E/\text{d}x} < 3$ $-0.126 < \sigma_{\text{TPC-d}E/\text{d}x} < 3$	$0 < \sigma_{\text{TPC-d}E/\text{d}x} < 3$	$0.126 < \sigma_{\text{TPC-d}E/\text{d}x} < 3$ $0.254 < \sigma_{\text{TPC-d}E/\text{d}x} < 3$
TPC-TRD-TOF analysis:			
Fixed electron efficiency for TRD likelihood cut	85%	80%	75%
TPC-EMCal analysis:			
Number of ITS hits	≥ 2	≥ 3	≥ 4
TPC dE/dx cut	$-2 < \sigma_{\text{TPC-d}E/\text{d}x} < 3$	$-1.5 < \sigma_{\text{TPC-d}E/\text{d}x} < 3$	$-1.5 < \sigma_{\text{TPC-d}E/\text{d}x} < 2$
E/p matching	$\lvert\sigma_{E/p}\rvert < 4$	$\lvert\sigma_{E/p}\rvert < 3$	$\lvert\sigma_{E/p}\rvert < 2$

TABLE IV. Overview over the contributions to the systematic uncertainties on the inclusive electron spectrum for the three analysis strategies.

Analysis	TPC-TOF	TPC-TRD-TOF	TPC-EMCal
p_t range (GeV/c)	0.5–4	4–8	3–7
Error source	Systematic uncertainty [%]		
Track matching	± 2	± 2	± 2
ITS number of hits	$p_t < 1.0$ GeV/c: $+4, -2$ $p_t > 1.0$ GeV/c: ± 2	± 5	± 10
TPC number of tracking clusters	$p_t < 1.1$ GeV/c: $+3, -6$ $p_t > 1.1$ GeV/c: ± 3	$p_t < 6$ GeV/c: ± 5 $p_t > 6$ GeV/c: ± 4	± 4
TPC number of PID clusters	± 2	$< \pm 1$	± 2
DCA to the primary vertex in xy (z)	$p_t < 0.6$ GeV/c: $+0.5, -2$ $p_t > 0.6$ GeV/c: $+0.5$	$< \pm 1$ $< \pm 1$	$< \pm 1$
TOF matching and PID	± 5	± 5	...
TPC PID	± 3	4 GeV/c $< p_t <$ 8 GeV/c: ± 10 $p_t > 8$ GeV/c: ± 16.7	± 6
TRD tracking and PID	...	± 5	...
EMCal PID	...	...	± 5
Electric charge	± 2	± 10	± 10
η	± 2	± 10	± 10
Unfolding	± 3	± 5	± 5

not point to the primary vertex. The total systematic uncertainty is calculated as the quadratic sum of all contributions, and it is of the order of 8.5% for the TPC-TOF and between 20 and 26% for the TPC-TRD-TOF parts of the spectrum, respectively.

2. TPC-EMCal analysis

Systematic uncertainties from the electron identification on the inclusive electron spectrum obtained with the TPC-EMCal approach arise from the dE/dx measured in the TPC and the E/p matching. The uncertainties were estimated by measuring the spectra with changing cuts on dE/dx and E/p. The variation of the cuts are summarized in Table III. The resulting uncertainty of the electron identification is 5% from the E/p matching, which includes the subtraction of contamination, and 6% from the dE/dx selection. The systematic uncertainties due to the track selection were estimated by applying the same variation of cuts as for the TPC-TOF/TPC-TRD-TOF analysis, except for the ITS cut. The individual contributions are summarized in Table IV. The total systematic uncertainty is approximately 20% on the inclusive electron spectrum.

H. Inclusive invariant p_t-differential electron yield

The electron yield per minimum bias pp collision was measured as a function of p_t. The hadron contamination was subtracted statistically from the spectrum and corrections for acceptance, reconstruction, and electron identification efficiency were applied. The corrected inclusive electron spectra measured with the TPC-TOF and TPC-TRD-TOF analyses are shown in the upper panel of Fig. 8. The spectra were parametrized simultaneously using a Tsallis function as depicted in Fig. 8. The results from both analyses agree well in the p_t region between 1 and 4 GeV/c as demonstrated in the lower panel of Fig. 8, which shows the ratios of the data to the common fit on a linear scale. However, the systematic uncertainties in the TPC-TOF analysis are substantially smaller than in the TPC-TRD-TOF analysis. Therefore, for the combined TPC-TOF/TPC-TRD-TOF inclusive yield the TPC-TOF result is used for $p_t < 4$ GeV/c. The extension towards higher p_t is given by the TPC-TRD-TOF measurement. The corresponding result employing the TPC-EMCal eID is also depicted in Fig. 8. Since the relevant material budget was not the same for the two approaches the contribution from photon conversions is different and, hence, the inclusive electron yield is larger for the TPC-EMCal analysis than for the TPC-TOF/TPC-TRD-TOF analysis.

I. Electron background cocktail

The inclusive electron spectrum can be subdivided into five components:

(1) signal heavy-flavor electrons, i.e., electrons from semileptonic decays of hadrons carrying a charm or beauty quark or antiquark,
(2) background electrons from Dalitz decays of light neutral mesons and from the conversion of decay photons in the material in the detector acceptance,
(3) background electrons from weak $K \rightarrow e\pi\nu$ (K_{e3}) decays and dielectron decays of light vector mesons,
(4) background electrons from dielectron decays of heavy quarkonia (J/ψ, Υ),

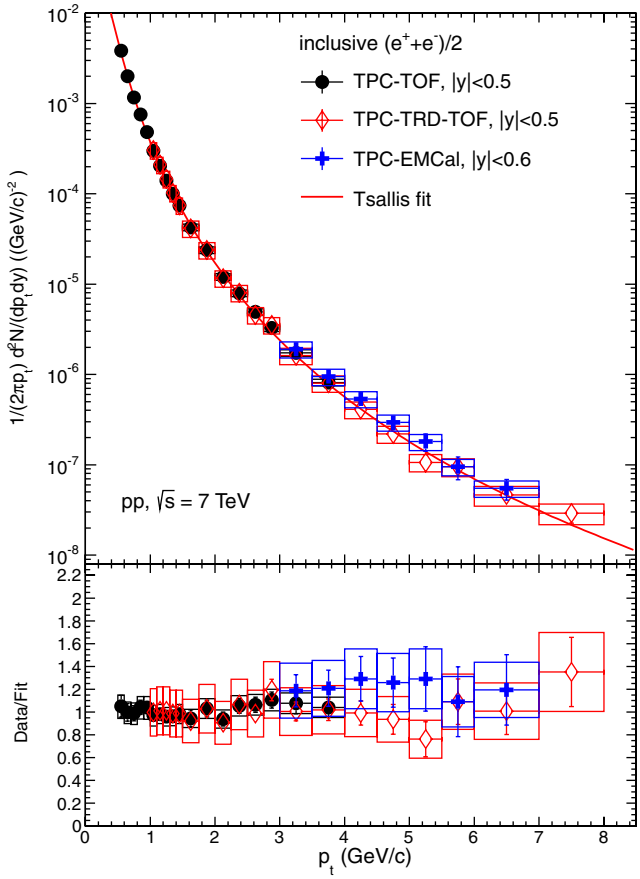

FIG. 8 (color online). Inclusive electron yield per minimum bias collision as function of p_t measured at midrapidity showing the TPC-TOF, TPC-TRD-TOF, and TPC-EMCal results, respectively, in pp collisions at $\sqrt{s} = 7$ TeV. The TPC-TOF and TPC-TRD-TOF spectra have been parametrized simultaneously using a Tsallis function (upper panel). The ratio of the measured spectra to the Tsallis fit is shown in the lower panel. Statistical uncertainties are indicated by error bars, while systematic uncertainties are shown as boxes.

(5) background electrons originating from partonic hard scattering processes. This includes electrons from the Drell-Yan process and electrons related to the production of prompt photons, i.e., both virtual prompt photons (electron-positron pairs) as well as real prompt photons which can convert in the material of the detector.

Of the background contributions listed above, the first one (Dalitz electrons and photon conversions in material) is the largest in electron yield. Toward high electron p_t, contributions from hard-scattering processes (prompt photons, decays of heavy quarkonia, and Drell-Yan processes) are important and will, eventually, become dominant.

The signal of electrons from heavy-flavor decays is small compared to the background at low p_t but rises with increasing p_t as will be shown in Sec. IV (Fig. 10). One technique to extract the heavy-flavor signal from the inclusive electron spectrum is the so-called "cocktail subtraction" method described in detail here. In this approach, a cocktail of electrons from different background sources was calculated using a Monte Carlo hadron-decay generator which, by construction, produces identical spectra for decay positrons and electrons. The resulting background spectra were then subtracted from the inclusive electron spectrum. This approach relies on the availability of the momentum distributions of the relevant background sources.

The most important background source is the neutral pion. The contribution from π^0 decays to the background is twofold. First, the Dalitz decay of neutral pions ($\pi^0 \to e^+e^-\gamma$, with a branching ratio BR of $1.174 \pm 0.035\%$ [11]) is a primary source of electrons from the collision vertex. Second, photons from the decay $\pi^0 \to \gamma\gamma$ (BR $= 98.823 \pm 0.034\%$ [11]) can convert in material into e^+e^- pairs in the ALICE acceptance. This process gives rise to a secondary source of electrons not originating from the collision vertex. It is important to point out that, although the total material budget in the ALICE central barrel acceptance is relatively large ($11.4 \pm 0.5\%$ of a radiation length X_0 integrated over a radial distance up to 180 cm from the beam line in the range $|\eta| < 0.9$) [36], the material budget relevant for the present analysis is much less (see below). In fact, electron candidate tracks considered here are required to be associated with either a hit in the first pixel layer of the ALICE ITS in case of the TPC-TOF/TPC-TRD-TOF analysis or a hit in any of the two pixel layers in the TPC-EMCal analysis. Therefore, only conversions in the beam pipe and in a fraction of the ITS material are relevant here. Consequently, the background contribution from photon conversions is similar to the contribution from Dalitz decays (see below for a detailed calculation).

The rapidity distribution of mesons is assumed to be flat around midrapidity. The momentum distributions of π^0 and η mesons are obtained via fitting the spectra as measured by the ALICE Collaboration [56]. In this measurement, π^0 and η decays in the $\gamma\gamma$ channel are reconstructed using two complementary techniques. As it is done conventionally, in the first approach the two decay photons are measured via electromagnetic calorimetry. This technique becomes notoriously difficult at low photon energy and, consequently, low meson p_t. In this region, it becomes advantageous to reconstruct photons in a second approach via the conversion into e^+e^- pairs in the detector acceptance. The large acceptance, high resolution ALICE TPC is ideally suited to perform such a measurement, which extends the π^0 spectrum down to 300 MeV/c. Combining the measurements via calorimetry and the reconstruction of photon conversions, the π^0 and η transverse momentum spectra from pp collisions at $\sqrt{s} = 7$ TeV were measured by ALICE over a wide p_t range [56].

The invariant differential cross section of π^0 and η meson production in pp collisions at $\sqrt{s} = 7$ GeV was parametrized with a Tsallis function [57] given by:

$$E\frac{\mathrm{d}^3\sigma}{\mathrm{d}p^3} = \frac{\sigma_{\mathrm{pp}}}{2\pi}\frac{\mathrm{d}N}{\mathrm{d}y}\frac{(n-1)(n-2)}{nT(nT+m(n-2))} \times (1+(m_{\mathrm{t}}-m)/(nT))^{-n}, \quad (2)$$

where the parameters $\mathrm{d}N/dy$, T, and n were obtained by fitting the experimental data as shown in Fig. 9, σ_{pp} is the inelastic pp cross section, m is the relevant meson's mass and m_{t} is the corresponding transverse mass $m_{\mathrm{t}} = \sqrt{m^2 + p_{\mathrm{t}}^2}$. The values of the fit parameters are listed in Table V.

Given that pion decays and the corresponding conversion of decay photons are the most important cocktail ingredient up to intermediate p_{t}, the systematic uncertainty of the background cocktail is dominated by the uncertainty of the pion input. To evaluate this uncertainty the measured differential pion cross section was moved up (down) in all p_{t} bins by the individual uncertainties in the bins, the parameterization according to Eq. (2) was repeated, and full cocktails were generated with these upper (lower) pion spectra as input. Thus, the uncertainty of the pion input was propagated to the electron cocktail. The same approach was followed for the η meson.

Other light mesons (ρ, ω, η', and ϕ) contribute to the background electron cocktail through their Dalitz and/or dielectron decay channels as well as through the conversion of photons from their decays. However, none of the contributions from these mesons is of any practical importance compared to the pion and the η meson. For the cocktail calculation, the shape of the invariant p_{t} distributions and the relative normalizations to the π^0 are required as input parameters for the heavier mesons. The shape of the p_{t} spectra was derived from the pion spectrum assuming m_{t} scaling, i.e., the spectral shapes of heavier mesons and pions were consistent as a function of m_{t}. Since the m_{t} scaling approach ensures that, at high p_{t}, the spectral shapes of all meson distributions are the same, the normalisation of the heavier meson spectra relative to the pion spectrum was determined by the ratios of heavier meson yields to neutral pion yields at high p_{t} (5 GeV/c in the present analysis). The values used are summarized in Table VI. The quoted systematic uncertainties correspond to conservative estimates of 30% on all meson-to-pion ratios, which were propagated to the corresponding contributions to the background electron spectrum.

A precise knowledge of the material budget is important for the calculation of the electron spectrum from photon conversions. An analysis of the reconstruction of photon conversions in ALICE demonstrated that the material budget implemented in the Monte Carlo simulation is in agreement within an uncertainty of 4.5% with the actual material budget of the experiment [36]. Since, for the present analysis, electron candidate tracks were required to be associated with a hit in the SPD, only the beam pipe, air, and a fraction of the ITS material contributed to the effective converter thickness. The beam pipe is made out of beryllium with a polyimide wrapping and its thickness in terms of radiation lengths is $X/X_0 = 0.26\%$. The corresponding thickness of a pixel layer is $X/X_0 = 1.14\%$ for the full layer, including the sensor, the readout chip, and the infrastructure [34]. The construction of the first pixel layer is such that the active sensor layer is closer to the beam line than the readout and most of the infrastructure, i.e., conversions in the latter do not give rise to a recorded hit in this detector. In the second pixel layer, the order is reversed, i.e., the readout and most of the infrastructure are closer to the beam line than the sensor itself. Therefore, for the TPC-EMCal analysis, the thickness of most of both pixel layers had to be considered in the calculation of the

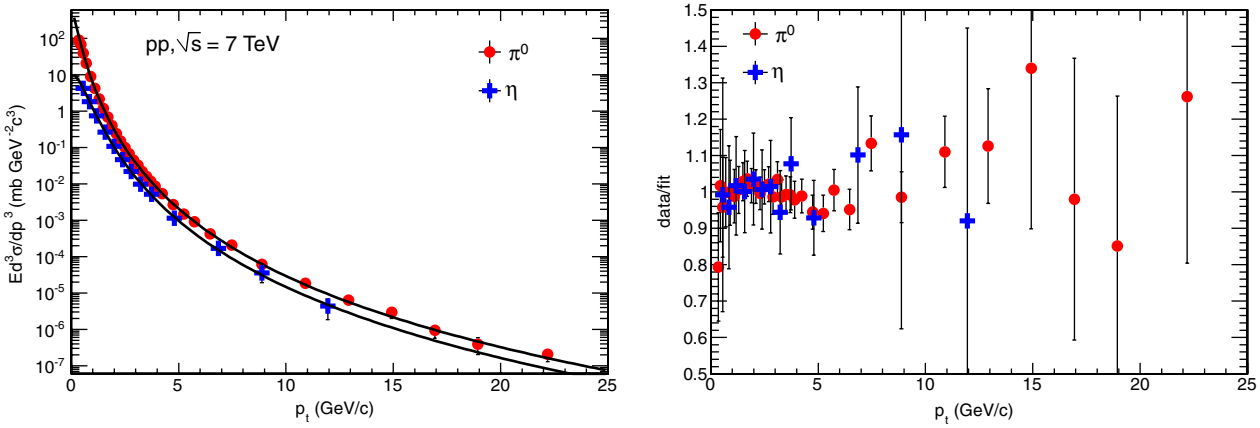

FIG. 9 (color online). Invariant differential production cross sections for neutral pions and η mesons in pp collision at $\sqrt{s} = 7$ TeV as function of p_{t} [56] together with fits using Eq. (2) (left panel). Ratios of the measured π^0 and η spectra to the fits (right panel). In both panels the error bars depict the combined statistical and systematic uncertainties of the neutral meson data.

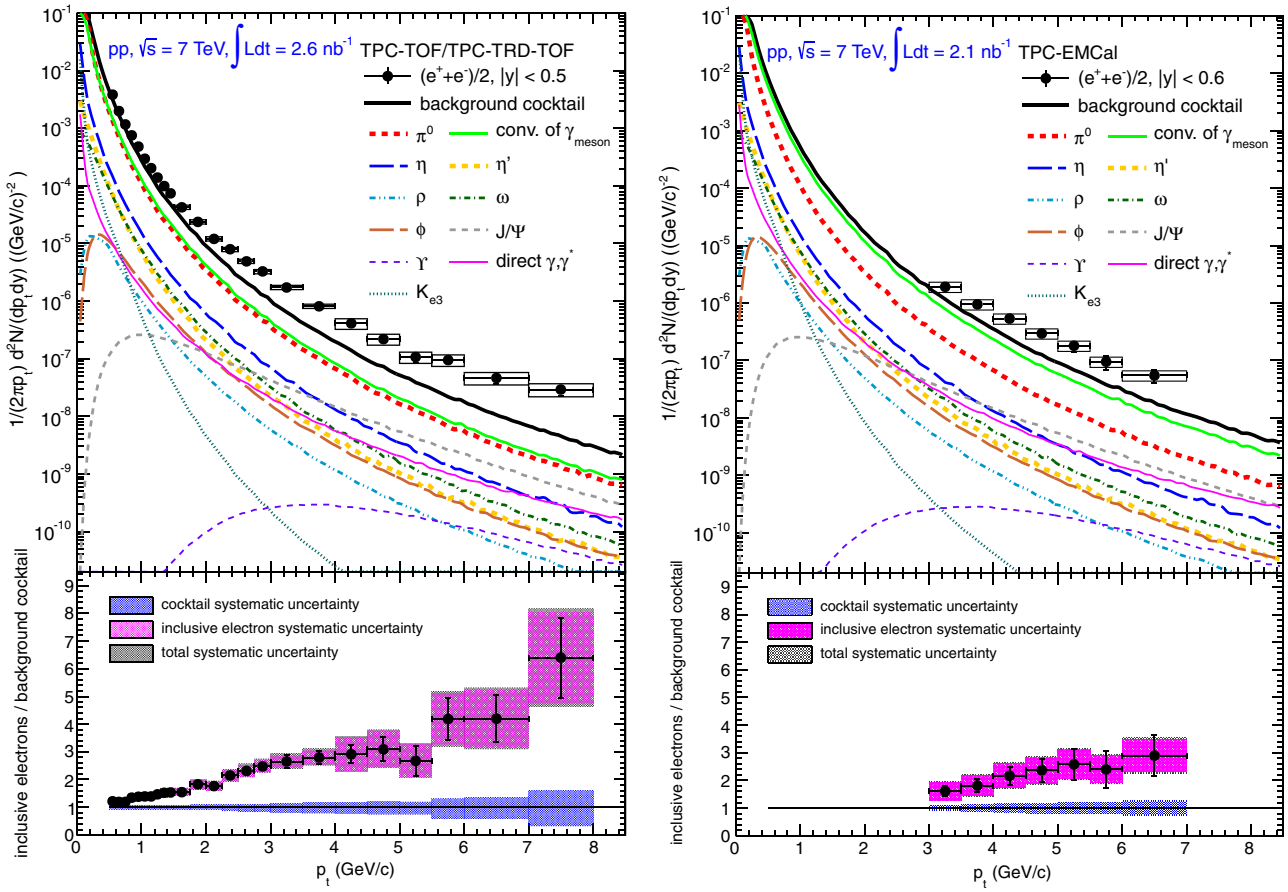

FIG. 10 (color online). Inclusive electron yield per minimum bias pp collision as function of p_t at $\sqrt{s} = 7$ TeV in comparison with background electron cocktails for the TPC-TOF/TPC-TRD-TOF analysis (left panel) and the TPC-EMCal analysis (right panel). Lower panels show the ratio of the inclusive electron yield to the background electron cocktail for both analyses.

electron background from photon conversions. Including an overall systematic uncertainty of 4.5% on the material budget [36], the resulting converter thickness was $X/X_0 = (2.15 \pm 0.11)\%$, including the beam pipe and air, for photons impinging perpendicularly on the beam pipe and the ITS, i.e., for photons at $\eta = 0$. For the TPC-TOF/TPC-TRD-TOF analysis, only a fraction of the first pixel layer was relevant in addition to the beam pipe and air. For the latter case, from the known material budget and from full Monte Carlo simulations of photon conversions in the pixel detector, the effective thickness of the first pixel layer was determined to be $(45 \pm 5)\%$ of its total thickness. Including the beam pipe and air, the effective converter thickness was $X/X_0 = (0.77 \pm 0.07)\%$ at $\eta = 0$. The geometric η dependence of the material budget was taken into account in the calculation of the photon conversion contribution in the electron background cocktail.

The ratio of conversion electrons to Dalitz electrons for π^0 decays was calculated as

$$\frac{\text{Conversion}}{\text{Dalitz}} = \frac{\text{BR}^{\gamma\gamma} \times 2 \times (1 - e^{-\frac{7}{9}\times\frac{X}{X_0}}) \times 2}{\text{BR}^{\text{Dalitz}} \times 2}, \qquad (3)$$

where $\text{BR}^{\gamma\gamma}$ and $\text{BR}^{\text{Dalitz}}$ are the branching ratios into the two-photon and Dalitz channels, respectively. For the TPC-TOF/TPC-TRD-TOF analysis, with $X/X_0 = (0.77 \pm 0.07)\%$, this ratio Conversion/Dalitz is equal to 1.01 ± 0.09. Due to the larger material budget relevant for the

TABLE V. Fit parameters of the Tsallis parametrization [see Eq. (2)] of the differential cross section of π^0 and η meson production.

Meson	dN/dy	T (MeV)	n
π^0	2.40 ± 0.15	139 ± 4	6.88 ± 0.07
η	0.21 ± 0.03	229 ± 21	7.0 ± 0.5

TABLE VI. Ratios of meson yields to neutral pion yields at $p_t = 5$ GeV/c in pp collisions at $\sqrt{s} = 7$ TeV.

$\rho/\pi^0 = 1.0 \pm 0.3$ [11]
$\omega/\pi^0 = 0.85 \pm 0.255$ [11,58]
$\eta'/\pi^0 = 0.25 \pm 0.075$ [11]
$\phi/\pi^0 = 0.40 \pm 0.12$ [11,59]

TPC-EMCal analysis, which is $X/X_0 = (2.15 \pm 0.11)\%$, the relative contribution from photon conversions to Dalitz decays was larger: Conversion/Dalitz $= 2.79 \pm 0.14$. For the decays of other light mesons the ratio is slightly smaller than for neutral pions due to the fact that $\mathrm{BR}^{\mathrm{Dalitz}}/\mathrm{BR}^{\gamma\gamma}$ increases with increasing parent meson mass.

In addition, it was taken into account that the photon conversion probability is not constant but depends slightly on the photon energy, introducing a p_{t} dependence of the ratio Conversion/Dalitz, which was determined in a full Monte Carlo simulation. The corresponding correction was applied in the calculation of the conversion contribution to the background electron cocktail. However, this correction is significant only for low momentum electrons ($0.5 < p_{\mathrm{t}} < 1$ GeV/c), where the ratio Conversion/Dalitz is reduced by 10% or less, relative to its asymptotic value given in Eq. (3).

The contribution from weak K_{e3} decays of charged and neutral kaons can only be determined via simulations, which take into account the geometry of the experimental apparatus, the reconstruction algorithms, and the electron identification cuts. It turned out that the contribution from K_{e3} decays to the inclusive electron spectrum was essentially negligible. This was due to the fact that electron candidates considered in the present analysis were required to be associated with a hit in the first pixel layer of the ALICE ITS. Since this detector layer is close to the primary collision vertex (3.9 cm radial distance from the beam line) and because of the rather long lifetime of the relevant kaons ($c\tau(\mathrm{K}^{\pm}) = 3.712$ m, $c\tau(\mathrm{K}^0_{\mathrm{L}}) = 15.34$ m [11]), only a tiny fraction of K_{e3} decays contributed to the background electron sample. For electrons with $p_{\mathrm{t}} = 0.5$ GeV/c the relative contribution from K_{e3} decays to the inclusive electron background was not more than 0.5%. For $p_{\mathrm{t}} = 1$ GeV/c this contribution decreased to $\approx 0.2\%$ and towards higher p_{t} it became even less. Given the limited statistics available in this simulation, a conservative systematic uncertainty of 100% is assigned to the K_{e3} contribution.

Electrons from the electromagnetic decays of heavy quarkonia have been added to the background electron cocktail based on measurements at the LHC. J/ψ production has been measured at midrapidity in pp collisions at 7 TeV by the ALICE [60,61] and CMS experiments [26]. A parametrization of these data, obtained by a simultaneous fit according to Eq. (2) was used as input for the cocktail generator. Υ production at midrapidity has been measured by the CMS experiment [62]. As for the J/ψ, the production cross section was parametrized and the decay contribution was included in the electron cocktail. While the contribution from J/ψ decays becomes relevant at high p_{t}, the Υ contribution is negligible for the electron cocktail in the current p_{t} range. While the systematic uncertainties of the measured production cross sections of heavy quarkonia were directly propagated to the corresponding decay electron spectra, their contribution to the systematic uncertainty of the latter is less than 1%.

Contributions to the background electron cocktail from prompt photons are twofold. Real photons produced in initial hard scattering processes, e.g., via quark-gluon Compton scattering, can convert in the detector material just as photons from meson decays. In addition, every source of real photons also emit virtual photons, i.e., electron-positron pairs. The spectrum of real prompt photons from an NLO pQCD calculation [63–65] using CTEQ6M5 parton distribution functions [66] with GRV parton-to-photon fragmentation functions [67,68] was parametrized, and the corresponding conversion electron spectrum was added to the background electron cocktail. The ratio of virtual prompt photons to real prompt photons increases with increasing p_{t} because the phase space for dielectron emission increases [69]. This has been taken into account in the calculation of the corresponding contribution to the background electron cocktail. Prompt photon production has not been measured in ALICE yet. Measurements at lower collision energy are in agreement with NLO pQCD calculations within uncertainties of significantly less than 50% at high p_{t} [70]. Conservatively, a systematic uncertainty of 50% was assigned to the contribution from prompt photons to the total background electron cocktail.

Contributions from the Drell-Yan process are expected to be small in the p_{t} range covered by the present analysis and, therefore, they were not included in the background electron cocktail.

TABLE VII. Overview of the contributions to the systematic uncertainties of the background cocktail. The contributions from mesons heavier than the η meson and the contribution from K_{e3} decays to the systematic uncertainty are less than 1% and, therefore, are not listed explicitly. For details on the error determination, see text.

p_{t} (GeV/c)	0.5	2	8
Error source	Systematic uncertainty (%)		
π^0 spectrum	± 8	± 4	± 8
γ conversions	± 4	± 4	± 3
η spectrum	± 1	± 1	± 4
prompt photons	$< \pm 1$	$< \pm 1$	± 4
Total	± 9	± 6	± 10

To calculate the systematic uncertainty of the cocktails, the systematic uncertainties of all uncorrelated cocktail ingredients were estimated as discussed above, propagated to the corresponding electron spectra, and added in quadrature. The cocktail systematic uncertainties are smallest in the p_t range between 1 and 2 GeV/c. The individual contributions and their dependence on p_t are summarized in Table VII, where error sources with less than 1% systematic uncertainty are not listed.

The total background cocktail electron cross sections were divided by the minimum bias pp cross section 62.2 ± 2.2(sys) mb [71] (see below) such that they can be directly compared to the measured inclusive electron yields per minimum bias triggered collision. These comparisons are shown in Fig. 10 for the TPC-TOF/TPC-TRD-TOF analysis (left panel) and the TPC-EMCal analysis (right panel).

IV. RESULTS AND DISCUSSION

A. Heavy-flavor hadron decay electron cross section

The differential inclusive electron yield in pp collisions at $\sqrt{s} = 7$ TeV, already shown in Fig. 8, is compared to the background electron yield as calculated within the cocktail approach in the left and right panels of Fig. 10 for the TPC-TOF/TPC-TRD-TOF and the TPC-EMCal analysis, respectively. Statistical uncertainties in the inclusive electron measurement are shown as error bars, while systematic uncertainties are indicated by boxes. The background contribution from photon conversions is smaller in the TPC-TOF/TPC-TRD-TOF analysis because in this case a hit in the first pixel layer is required for electron candidate tracks. Consequently, the ratio of the measured inclusive electron yield to the calculated electron background is larger for the TPC-TOF/TPC-TRD-TOF analysis than for the TPC-EMCal analysis as shown in the lower left and right panels of Fig. 10, respectively.

The differential production cross section of electrons from heavy-flavor decays is calculated by first subtracting the background cocktail from the inclusive electron spectrum and then multiplying the difference with the minimum bias pp cross section σ_{MB}. The corresponding systematic uncertainties propagated from the inclusive electron measurement and the electron background cocktail are summarized in Table VIII. The value for σ_{MB} is 62.2 ± 2.2(sys) mb. This number was obtained by relating σ_{MB} to the cross section σ_{VOAND} sampled with the V0AND trigger [71]. The latter corresponds to the coincidence between signals in the two VZERO detectors as measured in a van der Meer scan [72]. The relative factor $\sigma_{\mathrm{VOAND}}/\sigma_{\mathrm{MB}}$ is equal to 0.873 and stable within 1% over the analyzed data sample. The corresponding systematic uncertainty of 3.5% is due to uncertainties of the measured beam intensities and in the analysis procedure of the van der Meer scan [73]. As demonstrated in Fig. 11, the resulting cross sections from the TPC-TOF/TPC-TRD-TOF and TPC-EMCal analyses agree with each other within the experimental uncertainties.

Since the azimuthal coverages of the TRD and the EMCal are mutually exclusive and because the electron identification is done following different approaches, the statistical uncertainties of the inclusive electron spectra measured, using these two methods, are uncorrelated. While the systematic uncertainties related to the electron identification are essentially uncorrelated, those originating from the track reconstruction are mostly correlated. In addition, the systematic uncertainties of the electron background cocktails are correlated completely for both analyses.

The final production cross section for electrons from heavy-flavor hadron decays is calculated as the weighted average of the TPC-TOF/TPC-TRD-TOF and TPC-EMCal measurements, where the weights are calculated from the quadratic sums of the statistical and uncorrelated systematic uncertainties of the individual analyses. To determine the uncertainties of the weighted average, uncorrelated uncertainties of the two analyses are added in quadrature while correlated uncertainties are added linearly.

The differential invariant cross section of electrons from semileptonic heavy-flavor decays is measured for transverse momenta above 0.5 GeV/c. It is interesting to note that according to calculations using the PYTHIA 6.4.21 event generator [52] with the Perugia-0 parameter tuning [53] ~57% of the electrons from charm decays and ~73% of the electrons from beauty decays are within the measured p_t range in the rapidity interval $|y| < 0.5$. For FONLL [2,3,33] pQCD calculations, similar values are obtained. In this case, ~51% of the electrons from charm

TABLE VIII. Systematic uncertainties of the electron cross section from heavy-flavor hadron decays propagated from the inclusive electron measurement and the electron background cocktail for the TPC-TOF/TPC-TRD-TOF analysis. For $p_t = 3$, 5, and 7 GeV/c, the corresponding uncertainties for the TPC-EMCal analysis are quoted in parentheses.

p_t (GeV/c)	1	3	5	7
Error source	Systematic uncertainty (%)			
Inclusive electron spectrum	$^{+32}_{-36}$	±14(±53)	±33(±34)	±31(±31)
Electron background cocktail	$^{+17}_{-13}$	$^{+5}_{-3}$ ($^{+10}_{-11}$)	$^{+5}_{-4}$ (±5)	$^{+3}_{-2}$ (±5)
Total	$^{+36}_{-38}$	$^{+15}_{-14}$ (±54)	$^{+34}_{-33}$ (±35)	±31(±31)

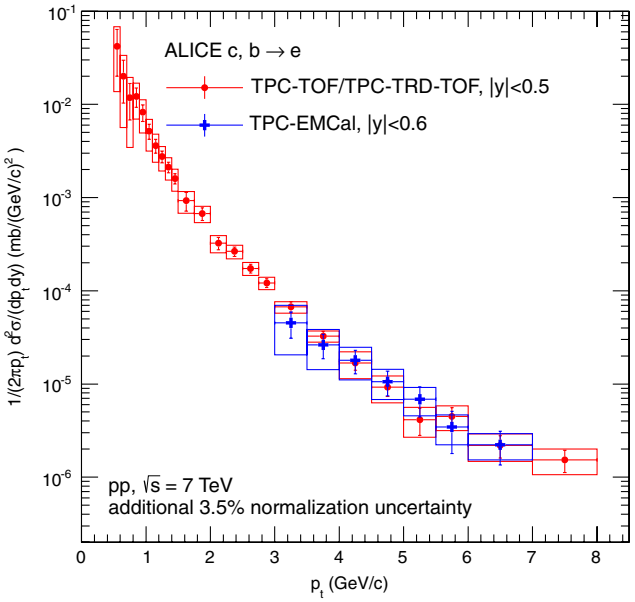

FIG. 11 (color online). Invariant differential production cross section for electrons from heavy-flavor decays in pp collisions at $\sqrt{s} = 7$ TeV for the TPC-TOF/TPC-TRD-TOF and the TPC-EMCal measurements. The overall systematic uncertainty of 3.5% on the cross section normalization is not included.

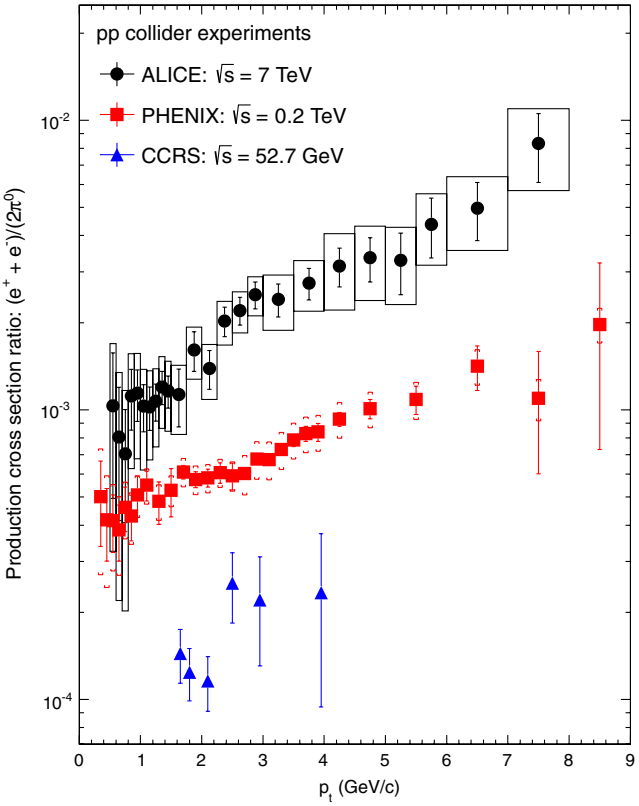

FIG. 12 (color online). Production cross section ratios of electrons from heavy-flavor hadron decays and neutral pions in pp collisions measured as function of p_t with ALICE at the LHC, PHENIX at RHIC [17,75–77], and the CCRS experiment at the ISR [12,74]. Error bars are statistical errors. Systematic uncertainties are depicted by boxes (ALICE) and brackets (PHENIX).

decays and ~90% of the electrons from beauty decays are within the accessible p_t range.

The ratio $(e^+ + e^-)/2\pi^0$ of the production cross sections of electrons from heavy-flavor hadron decays and π^0 mesons, which are the main source of background in the relevant p_t range, is depicted as a function of p_t in Fig. 12. The comparison with corresponding measurements from lower energy pp collider experiments demonstrates the different $\sqrt{s}$ dependence of the heavy- and light-flavor production cross sections. At the CERN ISR, the CCRS experiment recorded a first low statistics data sample of electrons from heavy-flavor hadron decays in pp collisions at $\sqrt{s} = 52.7$ GeV in the range $1.6 < p_t < 4.7$ GeV/c [12]. The charge-averaged inclusive charged pion production cross section was measured and parametrized by the British-Scandinavian Collaboration in the same collision system [74]. Assuming that the latter is equal to the neutral pion production cross section the ratio $(e^+ + e^-)/2\pi^0$ was calculated with substantial statistical uncertainties as shown in Fig. 12. At ISR energies, the ratio $(e^+ + e^-)/2\pi^0$ is of the order $(1–2) \times 10^{-4}$ without a significant p_t dependence in the range below 5 GeV/c, which is dominated by charm hadron decays. At $\sqrt{s} = 0.2$ TeV, production cross sections of both electrons from heavy-flavor hadron decays [17] and pions [75–77] have been measured with the PHENIX experiment in pp collisions at RHIC. The ratio $(e^+ + e^-)/2\pi^0$ was evaluated at given values of p_t in the range $0.3 < p_t < 9$ GeV/c as shown in Fig. 12. In the charm-hadron decay dominated low p_t region, the larger ratio $(e^+ + e^-)/2\pi^0 \approx 5 \times 10^{-4}$ is consistent with a more rapid increase of the charm production cross section with $\sqrt{s}$ as compared to the light-flavor production cross section. At RHIC, a pronounced p_t dependence of the ratio $(e^+ + e^-)/2\pi^0$ is observed. From the low p_t (~ 1 GeV/c) to the beauty-hadron decay dominated high p_t region (~ 9 GeV/c) $(e^+ + e^-)/2\pi^0$ rises by at least a factor of two, consistent with the beauty production cross section rising faster with $\sqrt{s}$ than the charm production cross section. At the LHC, the increase of the ratio $(e^+ + e^-)/2\pi^0$ with p_t is even larger. In the present measurement at $\sqrt{s} = 7$ TeV, $(e^+ + e^-)/2\pi^0$ grows by almost an order of magnitude from the charm decay dominated low p_t region to $\approx 10^{-2}$ in the beauty dominated high p_t region.

B. Comparison with FONLL pQCD

The measured differential invariant production cross section of electrons from heavy-flavor decays is compared with a FONLL pQCD calculation in Fig. 13, where error bars depict the statistical uncertainty while boxes show the total systematic uncertainty of the measurement. For the FONLL calculation CTEQ6.6 parton distribution functions

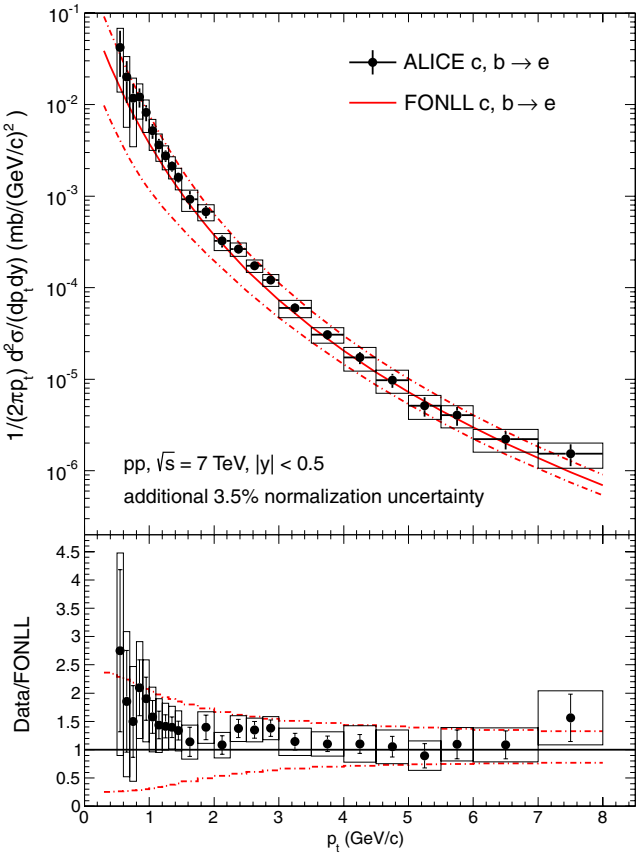

FIG. 13 (color online). The measured electron spectrum from heavy-flavor hadron decays is compared to a FONLL calculation for inclusive charm and beauty hadron semileptonic decays on an absolute scale in the upper panel. The ratio of the measured spectrum to the FONLL pQCD calculation is shown in the lower panel. Error bars, boxes, and theoretical uncertainties are described in the text.

[78] were used. To obtain the uncertainty of the calculation, indicated by dashed-dotted lines in Fig. 13, the factorisation and renormalization scales μ_F and μ_R, respectively, were varied independently in the ranges $0.5 < \mu_F/m_t < 2$ and $0.5 < \mu_R/m_t < 2$, with the additional constraint $0.5 < \mu_F/\mu_R < 2$, where m_t is the transverse mass of the heavy quarks. The charm quark mass was varied in FONLL within the range $1.3 < m_c < 1.7$ GeV/c^2 and the beauty quark mass was varied within $4.5 < m_b < 5.0$ GeV/c^2 [2]. For electrons from charm hadron decays, the contributions from D^0 and D^+ decays were weighted with the measured D^0/D^+ ratio [28]. Variations due to different choices of the parton distributions functions were also included in the theoretical uncertainty. The differential cross section of electrons from heavy-flavor decays in the rapidity interval $|y| < 0.5$ is shown in comparison with the FONLL prediction on an absolute scale in the upper panel of Fig. 13. In addition to charm and beauty hadron decays to electrons also the cascade beauty to charm to electron is included. Statistical and systematic uncertainties of the measurement are depicted as error bars and boxes, respectively. The cross section and uncertainty from FONLL are shown as solid and dashed-dotted lines, respectively.

The ratio of the measured cross section and the FONLL calculation is drawn in the lower panel of Fig. 13. Error bars and boxes around the data points indicate the statistical and systematic uncertainties of the electron spectrum from heavy-flavor decays, respectively. These systematic error boxes do not include any contribution from the FONLL calculation. The relative systematic uncertainties of the plotted ratio originating from the FONLL calculation is indicated by the dashed-dotted lines around one. Within substantial theoretical uncertainties the FONLL pQCD calculation is in agreement with the data.

C. ALICE and ATLAS measurements of electrons from heavy-flavor hadron decays

The ATLAS experiment has measured electrons from heavy-flavor decays in pp collisions at $\sqrt{s} = 7$ TeV in the p_t range $7 < p_t < 26$ GeV/c and in the rapidity interval $|y| < 2$, where the regions $1.37 < |y| < 1.52$ are excluded [25]. The p_t-differential production cross section, $d\sigma/dp_t$, published by ATLAS is divided bin by bin by $2\pi p_t \Delta y$,

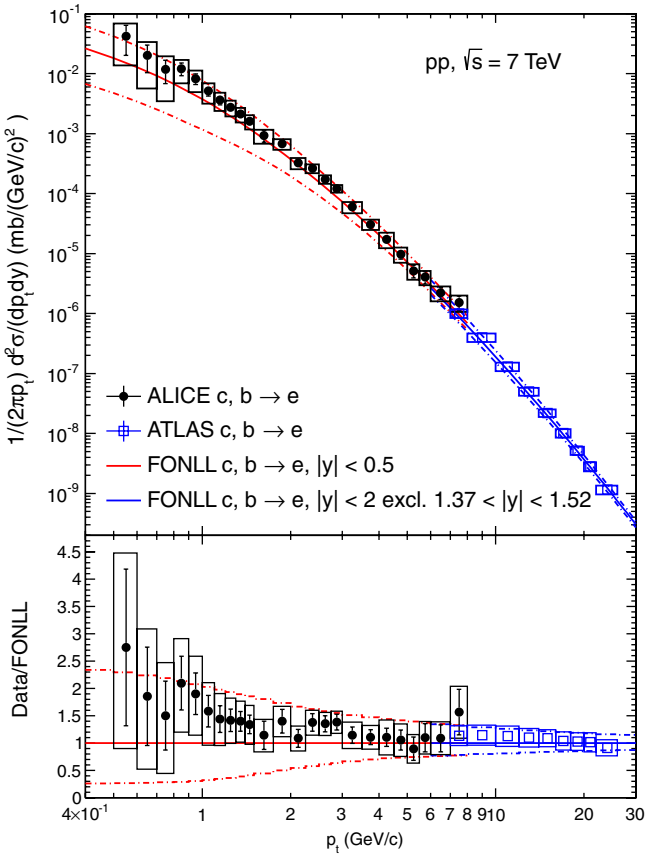

FIG. 14 (color online). Invariant differential production cross sections of electrons from heavy-flavor decays measured by ALICE and ATLAS [25] in pp collisions at $\sqrt{s} = 7$ TeV in different rapidity intervals (see text). FONLL pQCD calculations with the same rapidity selections are shown for comparison.

where p_t is the center of the individual transverse momentum bins chosen by ATLAS and Δy is the rapidity interval covered by the ATLAS measurement. The result is shown together with the electron cross section presented in this paper in Fig. 14. While the electron measurement by ALICE includes most of the total cross section, the data from ATLAS extend the measurement to higher p_t. Corresponding FONLL pQCD calculations in the rapidity intervals covered by ALICE and ATLAS, respectively, are included for comparison in Fig. 14 as well. Within the experimental and theoretical uncertainties FONLL is in agreement with both data sets. It should be noted that the invariant cross section per unit rapidity decreases with increasing width of the rapidity interval because the heavy-flavor production cross section decreases towards larger absolute rapidity values. However, this effect is small in pp collisions at $\sqrt{s} = 7$ TeV ($< 5\%$ for electrons from charm decays and $<10\%$ for electrons from beauty decays according to FONLL calculations).

V. SUMMARY

The inclusive differential production cross section of electrons from charm and beauty decays has been measured by ALICE in the transverse momentum range $0.5 < p_t < 8$ GeV/c at midrapidity in pp collisions at $\sqrt{s} = 7$ TeV. Within experimental and theoretical uncertainties a perturbative QCD calculation in the framework of FONLL is consistent with the measured differential cross section. The data presented in this paper extend a corresponding measurement from ATLAS, which is restricted to the high p_t region, toward substantially lower transverse momenta. This low p_t region includes the dominant fraction of the total heavy-flavor production cross section, and future higher-precision data might be sensitive to the parton distribution function of the proton at low x.

ACKNOWLEDGMENTS

The ALICE Collaboration would like to thank all its engineers and technicians for their invaluable contributions to the construction of the experiment and the CERN accelerator teams for the outstanding performance of the LHC complex. The ALICE Collaboration would like to thank M. Cacciari for providing the FONLL pQCD predictions for the cross sections of electrons from heavy-flavor hadron decays. Furthermore, the ALICE Collaboration would like to thank W. Vogelsang for providing the NLO pQCD predictions for direct photon production cross sections which were used as one of the inputs for the electron background cocktail. The ALICE Collaboration acknowledges the following funding agencies for their support in building and running the ALICE detector: Calouste Gulbenkian Foundation from Lisbon and Swiss Fonds Kidagan, Armenia; Conselho Nacional de Desenvolvimento Científico e Tecnológico (CNPq), Financiadora de Estudos e Projetos (FINEP), Fundação de Amparo à Pesquisa do Estado de São Paulo (FAPESP); National Natural Science Foundation of China (NSFC), the Chinese Ministry of Education (CMOE) and the Ministry of Science and Technology of China (MSTC); Ministry of Education and Youth of the Czech Republic; Danish Natural Science Research Council, the Carlsberg Foundation and the Danish National Research Foundation; The European Research Council under the European Community's Seventh Framework Programme; Helsinki Institute of Physics and the Academy of Finland; French CNRS-IN2P3, the "Region Pays de Loire," "Region Alsace," "Region Auvergne" and CEA, France; German BMBF and the Helmholtz Association; General Secretariat for Research and Technology, Ministry of Development, Greece; Hungarian OTKA and National Office for Research and Technology (NKTH); Department of Atomic Energy and Department of Science and Technology of the Government of India; Istituto Nazionale di Fisica Nucleare (INFN) of Italy; MEXT Grant-in-Aid for Specially Promoted Research, Japan; Joint Institute for Nuclear Research, Dubna; National Research Foundation of Korea (NRF); CONACYT, DGAPA, México, ALFA-EC and the HELEN Program (High-Energy Physics Latin-American-European Network); Stichting voor Fundamenteel Onderzoek der Materie (FOM) and the Nederlandse Organisatie voor Wetenschappelijk Onderzoek (NWO), Netherlands; Research Council of Norway (NFR); Polish Ministry of Science and Higher Education; National Authority for Scientific Research—NASR (Autoritatea Naţională pentru Cercetare Ştiinţifică—ANCS); Federal Agency of Science of the Ministry of Education and Science of Russian Federation, International Science and Technology Center, Russian Academy of Sciences, Russian Federal Agency of Atomic Energy, Russian Federal Agency for Science and Innovations and CERN-INTAS; Ministry of Education of Slovakia; Department of Science and Technology, South Africa; CIEMAT, EELA, Ministerio de Educación y Ciencia of Spain, Xunta de Galicia (Consellería de Educación), CEADEN, Cubaenergía, Cuba, and IAEA (International Atomic Energy Agency); Swedish Research Council (VR) and Knut & Alice Wallenberg Foundation (KAW); Ukraine Ministry of Education and Science; United Kingdom Science and Technology Facilities Council (STFC); The United States Department of Energy, the United States National Science Foundation, the State of Texas, and the State of Ohio.

[1] D. Acosta *et al.* (CDF Collaboration), Phys. Rev. Lett. **91**, 241804 (2003).
[2] M. Cacciari, M. Greco, and P. Nason, J. High Energy Phys. 05 (1998) 007.
[3] M. Cacciari, S. Frixione, and P. Nason, J. High Energy Phys. 03 (2001) 006.
[4] B. A. Kniehl, G. Kramer, I. Schienbein, and H. Spiesberger, Phys. Rev. Lett. **96**, 012001 (2006).
[5] D. Acosta *et al.* (CDF Collaboration), Phys. Rev. D **71**, 032001 (2005).
[6] I. Arsene *et al.* (BRAHMS Collaboration), Nucl. Phys. **A757**, 1 (2005).
[7] K. Adcox *et al.* (PHENIX Collaboration), Nucl. Phys. **A757**, 184 (2005).
[8] B. Back *et al.*, Nucl. Phys. **A757**, 28 (2005).
[9] J. Adams *et al.* (STAR Collaboration), Nucl. Phys. **A757**, 102 (2005).
[10] A. Adare *et al.* (PHENIX), Phys. Rev. Lett. **98**, 172301 (2007).
[11] K. Nakamura *et al.* (Particle Data Group), J. Phys. G **37**, 075021 (2010).
[12] F. Busser, L. Camilleri, L. Di Lella, B. Pope, A. Smith *et al.*, Phys. Lett. **53B**, 212 (1974).
[13] C. Albajar *et al.* (UA1 Collaboration), Phys. Lett. B **256**, 121 (1991).
[14] O. Botner, L. O. Eek, T. Ekelof, K. Fransson, A. Hallgren, P. Kostarakis, G. Lenzen, and B. Lund-Jensen, Phys. Lett. B **236**, 488 (1990).
[15] F. Abe, Phys. Rev. Lett. **71**, 500 (1993).
[16] S. Abachi *et al.* (D0 Collaboration), Phys. Rev. Lett. **74**, 3548 (1995).
[17] A. Adare *et al.* (PHENIX), Phys. Rev. C **84**, 044905 (2011).
[18] H. Agakishiev *et al.* (STAR), Phys. Rev. D **83**, 052006 (2011).
[19] A. Adare *et al.* (PHENIX), Phys. Rev. Lett. **97**, 252002 (2006).
[20] A. Adare *et al.* (PHENIX), Phys. Rev. Lett. **103**, 082002 (2009).
[21] M. M. Aggarwal *et al.* (STAR), Phys. Rev. Lett. **105**, 202301 (2010).
[22] S. S. Adler *et al.* (PHENIX), Phys. Rev. Lett. **94**, 082301 (2005).
[23] S. S. Adler *et al.* (PHENIX), Phys. Rev. Lett. **96**, 032301 (2006).
[24] B. I. Abelev *et al.* (STAR Collaboration), Phys. Rev. Lett. **106**, 159902 (2011).
[25] G. Aad *et al.* (ATLAS Collaboration), Phys. Lett. B **707**, 438 (2012).
[26] V. Khachatryan *et al.* (CMS Collaboration), Eur. Phys. J. C **71**, 1575 (2011).
[27] B. Abelev *et al.*, J. High Energy Phys. 11 (2012) 065.
[28] K. Aamodt *et al.* (ALICE Collaboration), J. High Energy Phys. 01 (2012) 128.
[29] B. Abelev *et al.* (ALICE Collaboration), J. High Energy Phys. 07 (2012) 191.
[30] B. Abelev *et al.* (ALICE Collaboration), Phys. Lett. B **708**, 265 (2012).
[31] B. Abelev *et al.* (ALICE Collaboration), Phys. Rev. Lett. **109**, 112301 (2012).
[32] S. Alekhin, G. Altarelli, N. Amapane, J. Andersen, V. Andreev *et al.*, arXiv:hep-ph/0601013.
[33] M. Cacciari, S. Frixione, N. Houdeau, M. L. Mangano, P. Nason, and G. RidolfiJ. High Energy Phys. 10 (2012) 137.
[34] K. Aamodt *et al.* (ALICE Collaboration), JINST **3**, S08002 (2008).
[35] K. Aamodt *et al.* (ALICE), JINST **5**, P03003 (2010).
[36] K. Koch *et al.* (ALICE Collaboration), Nucl. Phys. **A855**, 281 (2011).
[37] J. Alme *et al.*, Nucl. Instrum. Methods Phys. Res., Sect. A **622**, 316 (2010).
[38] A. Kalweit, Ph.D. thesis, Technical Unversity, Darmstadt, 2012.
[39] A. Andronic, Nucl. Instrum. Methods Phys. Res., Sect. A **558**, 516 (2006).
[40] C. Adler *et al.*, Nucl. Instrum. Methods Phys. Res., Sect. A **540**, 140 (2005).
[41] C. Adler *et al.*, Nucl. Instrum. Methods Phys. Res., Sect. A **540**, 140 (2005).
[42] A. Andronic *et al.*, Nucl. Instrum. Methods Phys. Res., Sect. A **498**, 143 (2003).
[43] A. Andronic *et al.*, Nucl. Instrum. Methods Phys. Res., Sect. A **525**, 447 (2004).
[44] C. Adler *et al.* (ALICE Collaboration), Nucl. Instrum. Methods Phys. Res., Sect. A **552**, 364 (2005).
[45] J. Klein (for the ALICE Collaboration), Nucl. Instrum. Methods Phys. Res., Sect. A (in press).
[46] A. Akindinov, A. Alici, P. Antonioli, S. Arcelli, M. Basile *et al.*, Eur. Phys. J. C **68**, 601 (2010).
[47] J. Allen *et al.*, Nucl. Instrum. Methods Phys. Res., Sect. A **615**, 6 (2010).
[48] P. Billoir, Nucl. Instrum. Methods Phys. Res., Sect. A **225**, 352 (1984).
[49] H. Bethe, Ann. Phys. (Berlin) **397**, 325 (1930).
[50] R. Bailhache and C. Lippmann, Nucl. Instrum. Methods Phys. Res., Sect. A **563**, 310 (2006).
[51] S. Gorbunov and I. Kisel (private communication).
[52] T. Sjostrand, S. Mrenna, and P. Skands, J. High Energy Phys. 05 (2006) 026.
[53] P. Z. Skands, Report No. FERMILAB-CONF-09-113-T, 2009.
[54] R. Brun *et al.*, CERN Program Library Long Write-up, Report No. W5013, 1994.
[55] J. Grosse-Oetringhaus, ALICE-INT-2008-002, 2008.
[56] B. Abelev *et al.* (ALICE Collaboration), Phys. Lett. B **717**, 162 (2012).
[57] C. Tsallis, J. Stat. Phys. **52**, 479 (1988).
[58] A. Adare *et al.*, Phys. Rev. C **84**, 044902 (2011).
[59] Y. Riabov (PHENIX Collaboration), J. Phys. G **34**, S925 (2007).
[60] K. Aamodt *et al.* (ALICE Collaboration), Phys. Lett. B **704**, 442 (2011).
[61] K. Aamodt *et al.* (ALICE Collaboration), Phys. Lett. B **718**, 692(E) (2012).
[62] V. Khachatryan *et al.* (CMS Collaboration), Phys. Rev. D **83**, 112004 (2011).
[63] L. Gordon and W. Vogelsang, Phys. Rev. D **48**, 3136 (1993).
[64] L. Gordon and W. Vogelsang, Phys. Rev. D **50**, 1901 (1994).
[65] W. Vogelsang (private communication).

[66] W. K. Tung, H. L Lai, A. Belyaev, J. Pumplin, D. Stump, and C.-P. Yuan, J. High Energy Phys. 02 (2007) 053.
[67] M. Gluck, E. Reya, and A. Vogt, Phys. Rev. D **48**, 116 (1993).
[68] M. Gluck, E. Reya, and A. Vogt, Phys. Rev. D **51**, 1427(E) (1995).
[69] A. Adare *et al.* (PHENIX Collaboration), Phys. Rev. C **81**, 034911 (2010).
[70] S. S. Adler *et al.* (PHENIX), Phys. Rev. Lett. **98**, 012002 (2007).
[71] B. Abelev *et al.* (ALICE Collaboration), arXiv:1208.4968.
[72] S. van der Meer, Report Nos. CERN-ISR-PO-68-31, ISR-PO-68-31, 1968.
[73] A. Alici *et al.*, Report No. CERN-ATS-Note-2011-016 PERF, 2011.
[74] B. Alper *et al.* (British-Scandinavian Collaboration), Nucl. Phys. **B87**, 19 (1975).
[75] S. S. Adler *et al.* (PHENIX Collaboration), Phys. Rev. Lett. **91**, 072301 (2003).
[76] A. Adare *et al.* (PHENIX Collaboration), Phys. Rev. Lett. **101**, 232301 (2008).
[77] S. S. Adler *et al.* (PHENIX Collaboration), Phys. Rev. C **69**, 034909 (2004).
[78] P. M. Nadolsky, H.-L. Lai, Q.-H. Cao, J. Huston, J. Pumplin, D. Stump, W.-K. Tung, and C.-P. Yuan, Phys. Rev. D **78**, 013004 (2008).